Computers and Geotechnics 175 (2024) 106638

Contents lists available at ScienceDirect

Computers and Geotechnics

journal homepage: www.elsevier.com/locate/compgeo

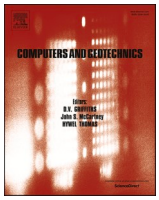

Research Paper

Horizontal bearing capacity of RC piles in cohesive soil: Numerical and theoretical modelling

Francesco Potini [a], Riccardo Conti [b,*]

[a] Niccolò Cusano University, Rome, Italy
[b] Università di Roma "Tor Vergata", Rome, Italy

ARTICLE INFO

Keywords:
Horizontal Loading
Finite Element Method
Concrete Damaged Plasticity
Limit Equilibrium
Design
Failure Envelope

ABSTRACT

This paper proposes a new method for computing the undrained lateral capacity of Reinforced Concrete (RC) piles in cohesive soils, overcoming inherent conservativeness of classical Broms' theory. The proposed method relies on a new theoretical distribution for the limiting soil resistance, simple enough to derive closed-form solutions of the undrained lateral capacity, for different restraints at the pile head and for all possible failure mechanisms. After validation against numerical results and experimental data, the model is used to compute the failure envelope of RC piles under generalised loading.

3D FE analyses are used as benchmark to identify the main factors governing the ultimate response of RC piles. To this purpose, the Concrete Damaged Plasticity model is adopted to reproduce nonlinear concrete behaviour, which is an essential ingredient when modelling pile behaviour under horizontal loading. FE analyses show that, contrary to what observed for rigid and elastic piles, the ultimate response of RC piles relies on the soil strength mobilised at shallow depths, where the normalised lateral soil resistance basically depends on the sole adhesion factor.

The proposed solutions are readily applicable to the design of single piles, as well as to the computation of three-dimensional interaction domains of pile groups.

1. Introduction

The horizontal bearing capacity of Reinforced Concrete (RC) piles is typically computed by means of limit equilibrium approaches, accounting for both the possible formation of plastic hinges within the pile (structural failure) and the activation of limit conditions in the surrounding soil (geotechnical failure). Among these, Broms' method (1964a,b) is still the most widespread in design practice, as it provides closed-form dimensionless solutions for the horizontal capacity of single piles embedded in granular and cohesive soils, based on simple assumptions on pile and soil behaviour. Recent studies have extended this method to the analysis of piles embedded in cohesive-frictional soils (Cecconi et al., 2019), also taking into account the possible increase of soil strength due to suction (Lalicata el al., 2023). In the case of purely cohesive soils, instead, the assessment of the undrained lateral capacity of piles still relies on the original Broms' solution, which considers a very simplified approximation of the limiting soil resistance and neglects any beneficial contribution provided by the adhesion at the soil-pile contact (Randolph and Houlsby, 1984; Murff and Hamilton, 1993; Georgiadis and Georgiadis, 2010).

Numerical Finite Element (FE) analyses, carried out applying a uniform horizontal displacement to a rigid vertical pile, have shown that the actual distribution of the undrained limiting soil resistance is a result of the interaction between two concurrent plastic mechanisms, *i.e.*: a two-dimensional (2D) plastic flow at large depth and a three-dimensional (3D) wedge failure close to the soil surface. In the former case, a very close approximation of the ultimate soil resistance was achieved combining 2D theoretical Upper-Bound (UB) and Lower-Bound (LB) solutions (Randolph and Houlsby, 1984; Martin and Randolph, 2006), while UB solutions were obtained in the latter case by considering more complex 3D plastic mechanisms (Murff and Hamilton, 1993; Yu et al., 2015). Based on theoretical and numerical outcomes, different expressions were proposed for the distribution of the undrained lateral soil resistance (Murff and Hamilton, 1993; Georgiadis and Georgiadis, 2010; Yu et al., 2015; Luo et al., 2021), usually adopted in standard *p-y* methods to compute the resistance of nonlinear springs distributed along the pile. Such distributions, however, are rarely used in design practice, as they require numerical integration procedures for

* Corresponding author.
E-mail addresses: francesco.potini@unicusano.it (F. Potini), riccardo.conti@uniroma2.it (R. Conti).

https://doi.org/10.1016/j.compgeo.2024.106638
Received 3 April 2024; Received in revised form 15 June 2024; Accepted 27 July 2024

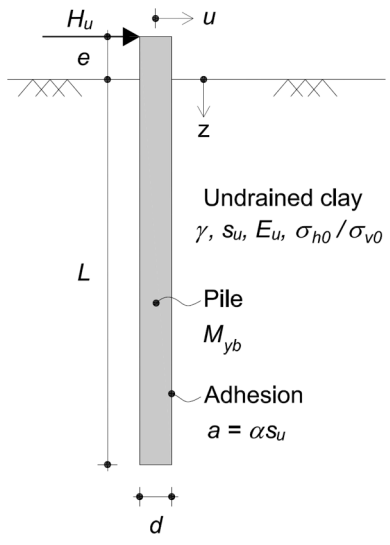

Fig. 1. Problem layout.

computing the lateral capacity of the pile with limit equilibrium methods.

Numerical 3D analyses were also carried out on horizontally loaded pile groups, always assuming a linear elastic behaviour for the piles (Comodromos and Pitilakis, 2005; Papadopoulou and Comodromos, 2010; Comodromos and Papadopoulou, 2012). While shedding light on the interaction mechanisms occurring within the group under working conditions, these studies cannot provide any valuable information on the ultimate pile response, corresponding to which structural failure always plays a major role. As a matter of fact, the need for a proper representation of the elastoplastic response of RC piles when investigating the pile-soil interaction up to failure was recently recognised by several studies, where the highly nonlinear behaviour of concrete under monotonic and cyclic loading was reproduced through advanced constitutive models developed within the realm of damage elasticity and hardening plasticity. Among these, Conte et al. (2013, 2015) tackled the problem of modelling the response of single RC piles in sandy soils under horizontal and inclined loads; Sakellariadis and Anastasopoulos (2022) and Psychari and Anastasopoulos (2022) analysed the ultimate response of pile groups under generalised loading; while Sakellariadis et al. (2020) dealt with the seismic response of piled foundations.

This work aims at providing a new approach for computing the undrained lateral capacity of piles in cohesive soils, overcoming inherent limitations of Broms' method. Based on a new simplified expression for the distribution of the limiting soil resistance, dimensionless closed-form solutions for the lateral bearing capacity are derived under different restraint conditions at the pile head. To this end, the results of advanced 3D FE analyses are used as benchmark to highlight the most relevant aspects concerning the ultimate response of RC piles under lateral loading, as well as to identify the main dimensionless factors governing such response. The proposed theoretical model is further validated against field and laboratory load test data available in the literature (Chen and Kulhawy, 1994) and its application for computing the analytical failure envelopes of single RC piles under generalised loading is thoroughly presented.

2. Problem definition and dimensional analysis

The case of a single RC pile with circular cross section (length, L; diameter, d; yielding moment, M_{yb}) embedded in a homogeneous overconsolidated clay layer (unit weight, γ; undrained shear strength, s_u; Young modulus in undrained conditions, E_u) is analysed (Fig. 1). In undrained conditions, the maximum horizontal load that can be applied at the pile head, H_u, is a function of (Broms, 1964a; Tzivakos and Kavvadas, 2014; Yu et al., 2015):

$$H_u = f\left(e, L, d, M_{yb}, \gamma, s_u, E_u, \alpha, \frac{\sigma_{h0}}{\sigma_{v0}}\right) \tag{1}$$

where e is the eccentricity of the horizontal load; σ_{h0}/σ_{v0} is the ratio between the horizontal and vertical geostatic total stress; and $0 \leq \alpha \leq 1$ is the adhesion factor, defined as the ratio between the adhesion at the pile-soil interface, a, and s_u ($a = \alpha \cdot s_u$).

Applying Buckingham's theorem, it is possible to rescale Eq. (1) in dimensionless form using d and s_u as dimensionally independent variables:

$$\frac{H_u}{s_u d^2} = F\left(\frac{e}{d}, \frac{L}{d}, \frac{M_{yb}}{s_u d^3}, \frac{E_u}{s_u}, \frac{\gamma d}{s_u}, \alpha, \frac{\sigma_{h0}}{\sigma_{v0}}\right) \tag{2}$$

The dimensionless ratios in Eq. (2) account for the mechanical, geometrical and physical factors affecting the lateral capacity of the pile, which in turn is governed by the mutual interaction between two possible failure mechanisms: (1) the formation of one or two plastic hinges along the pile (structural failure); and (2) the full attainment of the available soil shear strength (geotechnical failure), resulting in a three-dimensional wedge failure close to the soil surface, and a two-dimensional plastic flow at larger depth. Among these parameters: e/d takes into account possible moment loading applied to the pile head; L/d and $M_{yb}/s_u d^3$ primarily determine the actual number of plastic hinges occurring at failure (Broms, 1964b); E_u/s_u, $\gamma d/s_u$ and σ_{h0}/σ_{v0} influence the transition between the wedge and the flow-around plastic mechanisms (Tzivakos and Kavvadas, 2014; Yu et al., 2015; Luo et al., 2021); α affects the lateral limiting soil resistance (Randolph and Houlsby, 1984).

The numerical study presented in the following (Sections 3 and 4) will shed light on the actual relevance of the dimensionless ratios in Eq. (2), allowing to define a simple, yet accurate, theoretical model for the computation of both the ultimate soil resistance and the horizontal pile capacity (Section 5). To this end, different loading conditions and assumptions on pile behaviour will be considered, that is (Fig. 2): rigid pile subjected to a uniform horizontal displacement (R-U); elastic pile with a horizontal displacement applied at the top, which is free to rotate (EL-H); elastoplastic pile with a horizontal displacement applied at the top, where the rotation can be either free (EP-H) or restrained (EP-H-fix).

According to standard terminology, the pile will be referred to as 'free-head' and 'fixed-head', respectively, depending on the two restraint conditions applied at the head. In addition to this, depending on the structural failure mechanism, the pile will be referred to as: 'short' (zero plastic hinges); 'intermediate' (one plastic hinge, in the case of fixed-head pile); and 'long' (one (free-head) or two (fixed-head) plastic hinges).

3. Numerical FE model

A series of 3D total stress analyses of a single pile embedded in a uniform clay layer were carried out with the Finite Element (FE) code ABAQUS (Abaqus, 2017), assuming undrained conditions.

Fig. 3 shows the FE mesh adopted in this study, consisting of 8-nodes linear brick elements with reduced integration. Taking advantage of the problem symmetry, only half of the pile and soil domain were modelled. Moreover, based on a preliminary parametric study, mesh discretization and model dimensions were chosen in order not to affect the numerical results. Specifically, vertical boundaries were placed at a distance of $25d$ from the pile edge, while the bottom boundary is at a distance of $10d$ from the pile tip. Standard constraints were applied to the model boundaries, *i.e.*: normal displacements were restrained along the vertical boundaries, while all displacements were fixed at the base.

An initial geostatic stress state was applied within the soil domain by imposing a given ratio between horizontal and vertical total stresses, σ_{h0}/σ_{v0}. After this stage, a horizontal displacement was applied to the

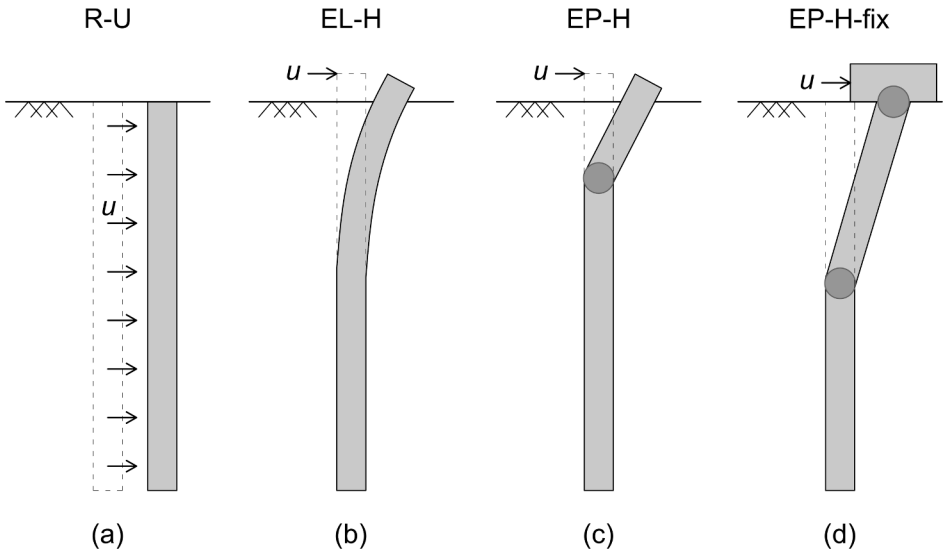

Fig. 2. Schematic representation of different pile loading and behaviour: (a) rigid pile under uniform horizontal displacement (R-U); (b) free-head elastic pile (EL-H); (c) free-head elastoplastic pile (EP-H); (d) fixed-head elastoplastic pile (EP-H-fix).

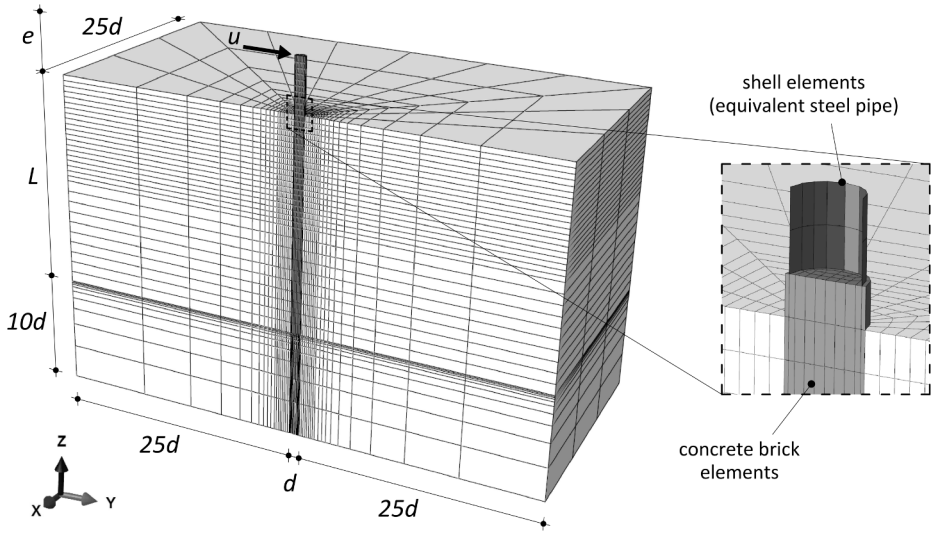

Fig. 3. FE model: 3D mesh and detail of the RC pile.

pile along the y-direction: a uniform displacement $u/d = 100$ % was prescribed for the rigid pile (R-U) in order to fully mobilise the soil resistance along the whole pile length (Yu et al., 2015), while a maximum displacement $u/d = 50$ % was applied at the head of the elastic (EL-H) and elastoplastic (EP-H) pile, enough to reach its lateral capacity in the latter case. Moreover, an additional constraint was applied to the top nodes of the fixed-head elastoplastic pile (EP-H-fix) to restrain the cross-section rotation.

Constitutive models for materials and soil-pile interface, as well as the modelling strategy for the elastoplastic pile, were chosen to provide a proper representation of all key features affecting the horizontal behaviour of RC piles at failure. Specifically, reinforcement bars were modelled as an equivalent steel pipe embedded in (and perfectly bonded to) the concrete continuum elements, using 4-nodes linear shell elements with reduced integration. Thickness (t_s) and diameter (d_s) of the circular steel pipe were chosen to have the same cross-sectional area (A_s) and moment of inertia (I_s) of the longitudinal discrete rebars, according to:

$$\begin{cases} A_s = \pi\left(R_e^2 - R_i^2\right) \\ I_s = \dfrac{\pi}{4}\left(R_e^4 - R_i^4\right) \end{cases} \tag{3}$$

where $R_i = (d_s\text{-}t_s)/2$ and $R_e = (d_s + t_s)/2$ are the internal and external radii of the equivalent tube, respectively. This choice allowed reproducing simply the overall confinement effect induced by transverse and longitudinal steel rebars in a real prototype RC pile, characterised by relatively high reinforcement ratios, $\rho = A_s/A_c$, where $A_c = \pi d^2/4$ is the area of the pile cross section.

3.1. Constitutive models

As standard in a total stress analysis, the undrained clay behaviour was modelled using a linear elastic-perfectly plastic model with a Tresca failure criterion and an associated flow rule (Comodromos and Papadopoulou, 2012; Georgiadis, 2014; Yu et al., 2015). The physical and constitutive parameters adopted for the soil are: the unit weight, γ (=20 kN/m^3); the Young modulus, E=E_u; the Poisson's ratio, $\nu = \nu_u$ (=0.495); the cohesion, $c = s_u$; the friction angle, $\phi = \phi_u$ (=0°); and the dilatancy

angle, ψ (=0°).

An isotropic elastic-perfectly plastic constitutive model was used for the reinforcement steel pipe, with a von Mises failure criterion and an associated flow rule. The physical and mechanical parameters were chosen to be representative of a B450C steel class, that is: unit weight, γ_s = 78 kN/m^3; Young modulus, E_s = 200 GPa; Poisson's ratio, ν_s = 0.3; and uniaxial yield strength, f_y = 450 MPa (Fig. 4a).

The mechanical behaviour of concrete was modelled through the Concrete Damaged Plasticity (CDP) model (Lubliner et al., 1989; Lee and Fenves, 1998), which combines key features of isotropic damage elasticity and hardening plasticity to reproduce the inelastic behaviour of quasi-brittle materials under monotonic and cyclic loading. The model equations in the plastic regime are firstly formulated under uniaxial loading and then extended to multiaxial conditions. As an example, Fig. 4b shows the stress–strain response assumed in this work under uniaxial tension and compression, representative of a C25/30 concrete class. In tension, the material behaviour is linear elastic until the uniaxial tensile yield stress (f_{t0}) is reached, beyond which softening occurs. The stress–strain response in compression, instead, is linear elastic until the compressive yield stress, f_{c0}, beyond which a hardening behaviour is assumed until the ultimate stress, f_{cu}; beyond f_{cu}, the material response follows a softening branch until complete failure due to crushing. The complete set of evolution equations are briefly recalled in Appendix A, while Table 1 summarises the physical and constitutive parameters adopted in this study for the concrete: the dilatancy angle, ψ, and the eccentricity parameter, ϵ, define the flow rule; f_{c0} and f_{b0} are the initial yield stresses under uniaxial and biaxial compression, respectively; K_c controls the shape of the yield surface in triaxial compression; μ_{visc} is a viscosity parameter, which allows regularizing the evolution laws in the highly-nonlinear regime, following the viscoplastic formulation of Duvaut-Lions type (Duvaut and Lions, 1972).

The pile-soil interface was modelled with tensionless contact elements, which allow both sliding and separation. An elastoplastic frictional behaviour was assumed for the interface, with the shear strength defined as:

$$\tau_{lim} = \mu \bullet \sigma_n (\leq \tau_{max}) \quad (4)$$

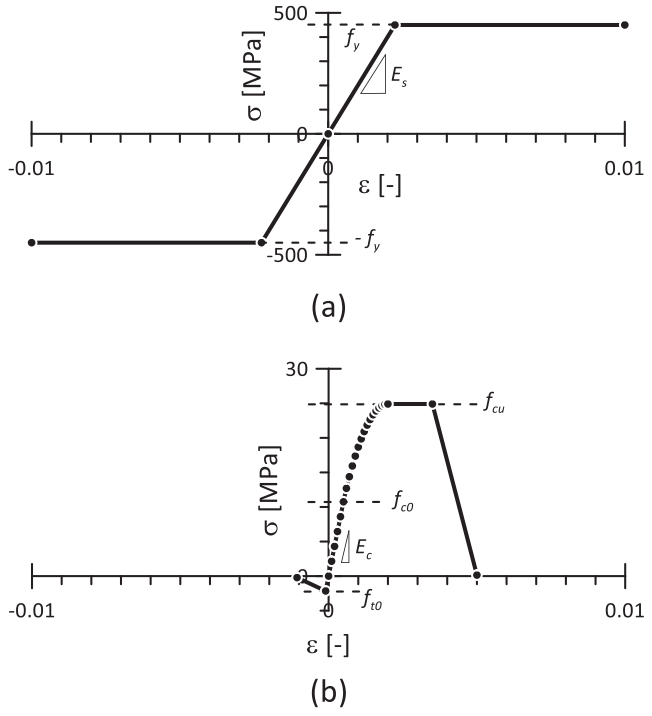

Fig. 4. Uniaxial stress–strain response adopted for (a) steel and (b) concrete.

Table 1
Physical and constitutive parameters adopted for the CDP model.

γ_c [kN/m^3]	E_c [GPa]	ν_c	ψ [°]	ϵ	f_{b0}/f_{c0}	K_c	μ_{visc}
25	21.5	0.15	30	0.1	1.16	0.667	10^{-4}

where σ_n is the normal stress acting on the interface, μ is the friction coefficient and τ_{max} is a threshold value for the maximum allowable shear strength. Similar to what implemented by Psychari and Anastasopoulos (2022), in order to achieve a virtual cohesive behaviour of the interface along the whole pile length, a relatively high value of the friction coefficient was adopted (μ = 2), together with $\tau_{max} = \alpha s_u$. where α is the interface adhesion factor.

3.2. Parametric study

The numerical parametric study comprised a total of 56 3D FE analyses, as summarised in Table 2. A first set of analyses (# 1–41) was carried out to investigate the dependence of the limiting soil resistance and of the horizontal pile capacity on the dimensionless factors $\gamma d/s_u$ (=0.1 ÷ 0.8), E_u/s_u (=100 ÷ 500), σ_{h0}/σ_{v0} (=0.5 ÷ 1.5) and α (=0 ÷ 1), whose values were chosen to be representative of bored RC piles in overconsolidated clayey soil deposits. At this stage, different loading conditions (uniform displacement, free-head and fixed-head pile) and pile behaviour (rigid, elastic, elastoplastic) were assumed, while always referring to a relatively long pile (L=40 m), to allow for a clear identification of the soil resistance profile down to a sufficient depth. A second set of analyses (# 42–56) was then carried out to validate the proposed theoretical model for the computation of the horizontal pile capacity against 3D FE models representative of free-head and fixed-head RC piles. For all EP-H and EP-H-fix models, the equivalent steel pipe was characterised by a reinforcement ratio ρ = 1.8 % and a diameter d_s = 0.9·d.

3.3. Model validation

The structural model of RC piles, as well as the constitutive assumption adopted for the pile-soil interface, were validated against two reference model tests, corresponding to which theoretical solutions are available. Specifically, the simple case of a cantilever beam loaded by a concentrated load at the free edge was used to validate the structural model, while plane-strain 2D analyses were implemented to assess the capability of the adopted interfaces to reproduce pile-soil interaction at failure.

3.3.1. Structural behaviour of RC piles

As shown in Fig. 5, a circular RC cantilever beam with the left-hand fixed was analysed (L=10 m, d = 1.0 m, d_s/d = 0.9, ρ = 1.8 %). An axial load, N, was applied at the right-hand edge, followed by a transversal displacement, v, up to the attainment of the ultimate bending condition.

FE results were validated against the theoretical outcomes provided by the fiber element method (Ceresa et al., 2007). The latter is based on the discretization of the beam cross-section in a series of fibers, under two fundamental assumptions: (i) cross-sections remain plane and normal to the deformed longitudinal axis (Euler-Bernulli approach), and (ii) perfect grip between longitudinal rebars and concrete. Using the uniaxial constitutive relationships displayed in Fig. 4a,b for steel and concrete, respectively, the behaviour of the circular beam under axial force and uniaxial moment was computed by integrating the fiber stresses over the cross-section.

The overall structural behaviour is illustrated in Fig. 6, showing: (a) the longitudinal strain contours (ε_z, positive in tension, negative in compression) computed within the concrete elements at different values of v (N=5 MN); (b) the numerical and theoretical moment-displacement curves, at different values of N; (c) the N-M interaction diagram at

Table 2
3D FE analyses carried out in the parametric study.

Analysis #	L m	d m	s_u kPa	L/d –	e/d –	$\gamma d/s_u$ –	E_u/s_u –	$M_y/s_u d^3$ –	σ_{h0}/σ_{v0} –	α –	type of loading / pile
1–3	40	1.0	100	40	–	0.2	100, 200, 500	–	1	0.5	uniform / rigid (R-U)
4–5	40	1.0	100	40	–	0.2	200	–	0.5, 1.5	0.5	
6	40	1.0	75	40	–	0.27	200	–	1	0.5	
7–9	40	1.0	50	40	–	0.4	100, 200, 500	–	1	0.5	
10–11	40	1.0	50	40	–	0.4	200	–	0.5, 1.5	0.5	
12–13	40	1.0	50	40	–	0.4	200	–	1	0, 1	
14	40	1.0	50	40	0	0.4	200	–	1	0.5	free-head / elastic (EL-H)
15	40	1.0	75	40	0	0.27	200	–	1	0.5	
16–18	40	1.0	100	40	0	0.2	100, 200, 500	–	1	0.5	
19–20	40	1.0	100	40	0	0.2	200	–	0.5, 1.5	0.5	
21	40	0.5	50	80	0	0.2	200	–	1	0.5	
22	40	0.8	50	50	0	0.32	200	–	1	0.5	
23	40	1.5	50	27	0	0.6	200	–	1	0.5	
24	40	2.0	50	20	0	0.8	200	–	1	0.5	
25–27	40	1.0	50	40	0	0.4	200	56.5	1	0, 0.5, 1	free-head / elastoplastic (EP-H)
28	40	1.0	75	40	0	0.27	200	37.7	1	0.5	
29–31	40	1.0	100	40	0	0.2	100, 200, 500	28.2	1	0.5	
32–33	40	1.0	100	40	0	0.2	200	28.2	0.5, 1.5	0.5	
34	40	1.0	150	40	0	0.13	200	18.8	1	0.5	
35	40	0.5	50	40	0	0.2	200	56.5	1	0.5	
36	40	0.8	50	40	0	0.32	200	56.5	1	0.5	
37	40	1.5	50	40	0	0.6	200	56.5	1	0.5	
38	40	2.0	50	40	0	0.8	200	56.5	1	0.5	
39–41	40	1.0	100	40	0	0.2	100, 200, 500	28.2	1	0.5	fixed-head / elastoplastic (EP-H-fix)
42	20	1.0	141	20	0	0.14	200	20.0	1	0.5	free-head / elastoplastic (EP-H)
43	20	1.0	56	20	0	0.35	200	50.0	1	0.5	
44	20	1.0	28	20	0	0.71	200	100.0	1	0.5	
45	20	1.0	141	20	5	0.14	200	20.0	1	0.5	
46	20	1.0	56	20	5	0.35	200	50.0	1	0.5	
47	20	1.0	28	20	5	0.71	200	100.0	1	0.5	
48	20	1.0	141	20	15	0.14	200	20.0	1	0.5	
49	20	1.0	56	20	15	0.35	200	50.0	1	0.5	
50	20	1.0	28	20	15	0.71	200	100.0	1	0.5	
51	5	1.0	141	5	0	0.14	200	20.0	1	0.5	fixed-head / elastoplastic (EP-H-fix)
52	7	1.0	56	7	0	0.35	200	50.0	1	0.5	
53	10	1.0	28	10	0	0.71	200	100.0	1	0.5	
54	20	1.0	141	20	0	0.14	200	20.0	1	0.5	
55	20	1.0	56	20	0	0.35	200	50.0	1	0.5	
56	20	1.0	28	20	0	0.71	200	100.0	1	0.5	

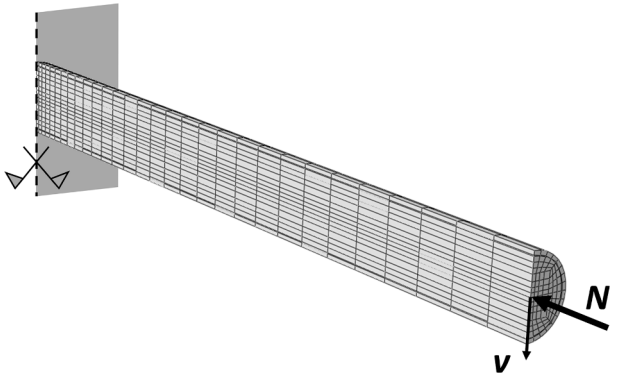

Fig. 5. RC cantilever beam: FE mesh and boundary conditions.

failure. As expected, as v increases, the concrete under tension cracks, until structural failure occurs and a plastic hinge forms close to the fixed edge of the beam (Fig. 6a). The comparison between numerical and theoretical $M-v$ curves is quite satisfactory, confirming the capability of the CDP model to well reproduce the dependency of the moment capacity of the RC section on the applied axial load (Fig. 6b). A slight difference between the two models is observed at failure, where, due to the confinement effect induced by the steel pipe and the plane-stress formulation of the shell elements, the FE model exhibits higher ductility and moment capacity compared with the theoretical one, which is formulated under pure uniaxial conditions. As a result, the numerical *N-M* interaction diagram is slightly larger than the theoretical one, as shown in Fig. 6c.

3.3.2. 2D limiting soil pressure on a circular pile

Plane-strain 2D analyses were carried out on a single pile ($d = 1$ m) in a cohesive soil ($s_u = 100$ kPa; $E_u/s_u = 200$; $\sigma_{v0} = 500$ kPa; $\sigma_{h0}/\sigma_{v0} = 1$), subjected to a pure horizontal displacement in undrained conditions, considering different values of the interface adhesion factor ($\alpha = 0$, 0.25, 0.5, 0.75, 1). FE results were interpreted in terms of the dimensionless contact pressure $\bar{p}_{u,2D} = p_{u,2D}/s_u d$, where $p_{u,2D}$ is the limiting soil resistance (per unit length), including the contribution of both normal and shear stresses at the pile-soil interface.

Fig. 7a shows a comparison between the numerical values of $\bar{p}_{u,2D}$ and the UB and LB solutions provided by Martin and Randolph (2006) and Randolph and Houlsby (1984), respectively, the latter given by the expression:

$$\bar{p}_{u,2D} = \pi + 2\Delta + 2\cos\Delta + 4\left[\cos\left(\frac{\Delta}{2}\right) + \sin\left(\frac{\Delta}{2}\right)\right] \quad (5)$$

where $\Delta = \sin^{-1}\alpha$. For $\alpha = 0$ (smooth contact) the results are virtually the same, while a small difference appears with increasing the adhesion factor, reaching a maximum value of 2.5 % for the case $\alpha = 1$ (rough contact). This result is due to a gap formation at the pile-soil contact in the FE model (behind the pile with respect to the applied displacement), where contact stresses are null, not taken into account in the theoretical solutions.

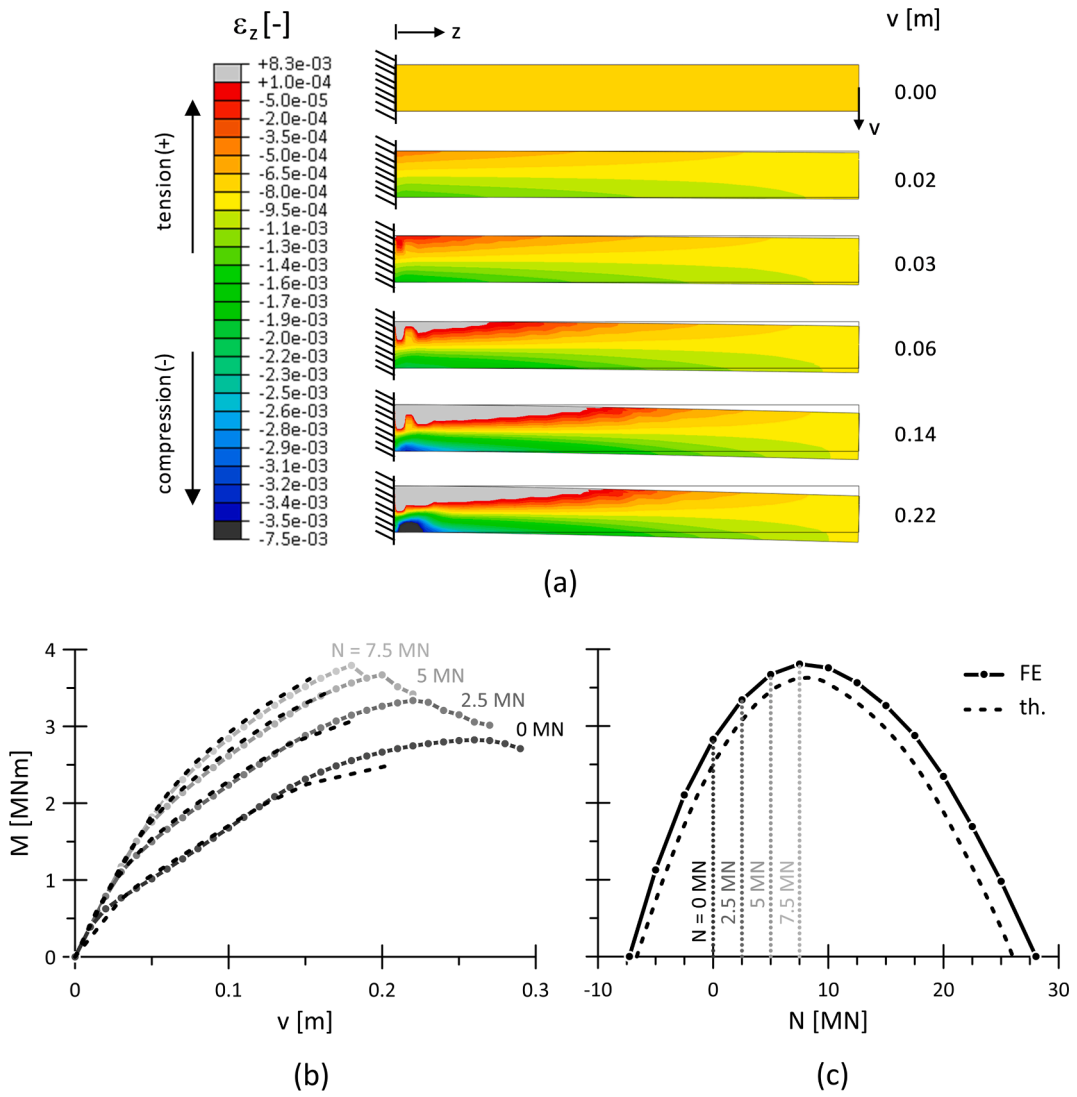

Fig. 6. RC cantilever beam: (a) longitudinal strain contours at different transversal displacements (N=5 MN); (b) numerical and theoretical $M-v$ curves and (c) N-M interaction diagram at $z = 0$ m.

Fig. 7b shows the contours and vectors of soil displacements computed for $\alpha = 0$, 0.5 and 1. In perfect agreement with the UB solution proposed by Martin and Randolph (2006), a "flow-around" plastic mechanism developed within the soil, characterised by the formation of a fan shear zone all around the pile. Consistently with the theoretical model, the mobilization of shear stresses at the pile-soil interface ($\alpha \neq 0$) induces the formation of a rigid zone in front of the pile; also, the soil volume involved in the plastic mechanism increases with increasing α.

4. Numerical FE results

4.1. Limiting soil resistance

Fig. 8 shows the profiles of dimensionless contact pressures, $\bar{p}_u = p_u/s_u d$, computed for the case of uniformly loaded rigid pile (R-U), by varying the dimensionless ratios: (a) $\gamma d/s_u$ ($E_u/s_u = 200$, $\sigma_{h0}/\sigma_{v0} = 1$, $\alpha = 0.5$); (b) E_u/s_u ($\gamma d/s_u = 0.20$–0.40; $\sigma_{h0}/\sigma_{v0} = 1$, $\alpha = 0.5$); and (c) σ_{h0}/σ_{v0} ($\gamma d/s_u = 0.20$–0.40; $E_u/s_u = 200$, $\alpha = 0.5$). For the sake of comparison, Fig. 8 also displays three literature solutions derived from the best fit of 3D FE analyses (Georgiadis and Georgiadis, 2010), FE Limit Analysis (Luo et al., 2021), and 3D UB solutions (Yu et al., 2015), respectively. As shown by several authors (Murff and Hamilton, 1993; Georgiadis and Georgiadis, 2010; Yu et al., 2015), the applied uniform displacement allows for a full attainment of the soil resistance along the entire pile shaft, comprising the wedge failure mechanism in the near surface and the mobilization of the flow-around limiting resistance at larger depth, where numerical FE results match the theoretical LB solution derived by Randolph and Houlsby (1984). As apparent from the figure, the $\gamma d/s_u$, E_u/s_u and σ_{h0}/σ_{v0} ratios have similar effects, inducing slight variations of both the ultimate soil resistance in the wedge failure zone and the transition depth at which the flow-around mechanism is activated. These ratios, however, do not affect the distribution of the limiting soil pressure at shallow depth ($z/d \leq 2 \div 3$). Numerical FE results are in very good agreement with the theoretical distributions of $\bar{p}_u$, with minor differences due to the fact that simplified literature solutions do not depend on the ratios E_u/s_u and σ_{h0}/σ_{v0}.

When moving to the case of free-head elastic (EL-H) and elastoplastic (EP-H) piles, the resulting displacements are not sufficient neither for activating the plastic flow at depth nor for fully mobilising the soil resistance in the wedge failure mechanism (Fig. 9). Moreover, the pile deflection induces an inversion in the soil contact pressures, which occurs approximately at $z/d \approx 11 \div 12$ and $z/d \approx 5 \div 6$ for the EL-H and EP-H pile, respectively. In the latter case, the soil volume involved in the plastic mechanism is significantly reduced due to the formation of a plastic hinge within the structural element, below which the pile does not exhibit significant displacements. Likewise to what observed under a

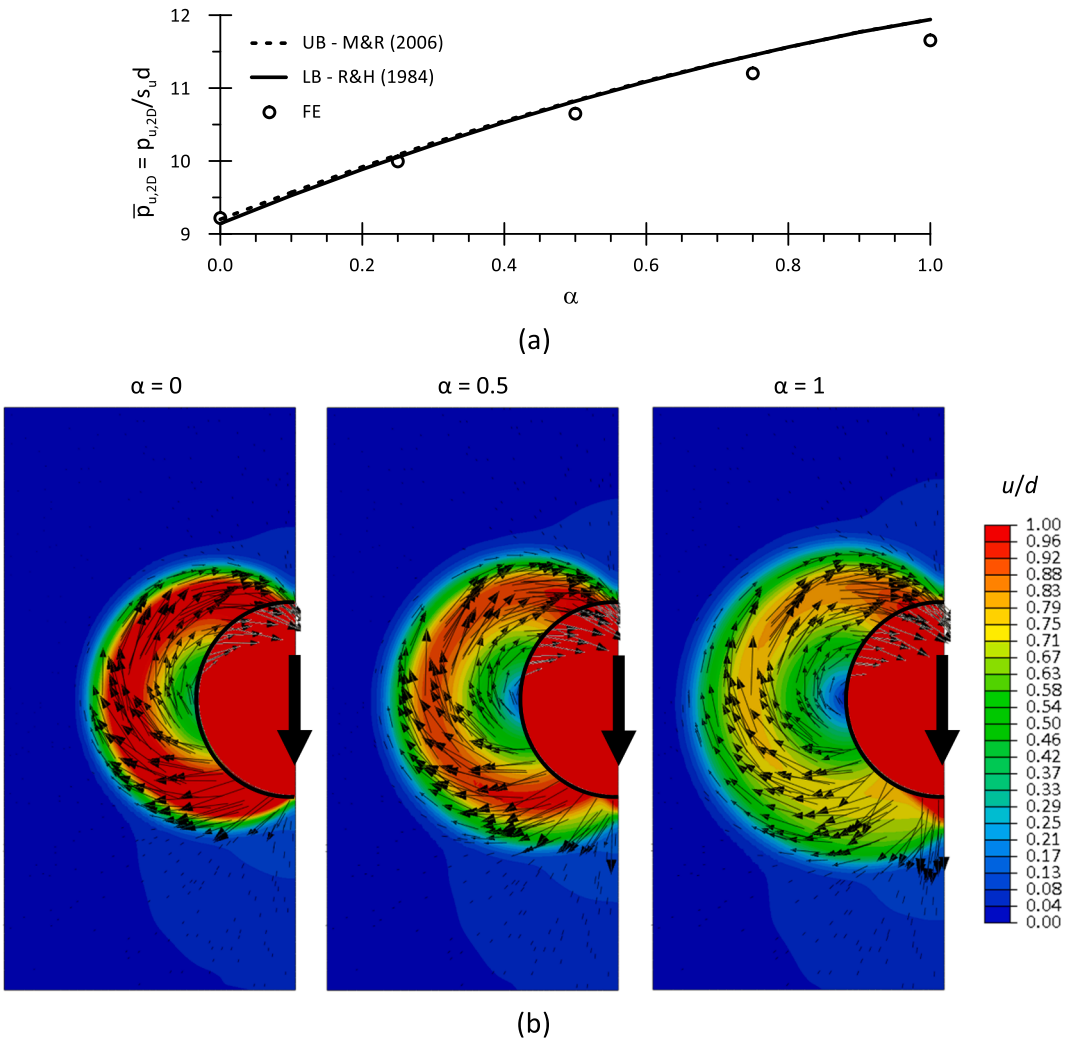

Fig. 7. Plane-strain 2D analyses: (a) normalised limiting soil resistance $\overline{p}_{u,2D}$; (b) contours and vectors of soil displacements computed for α = 0, 0.5 and 1.

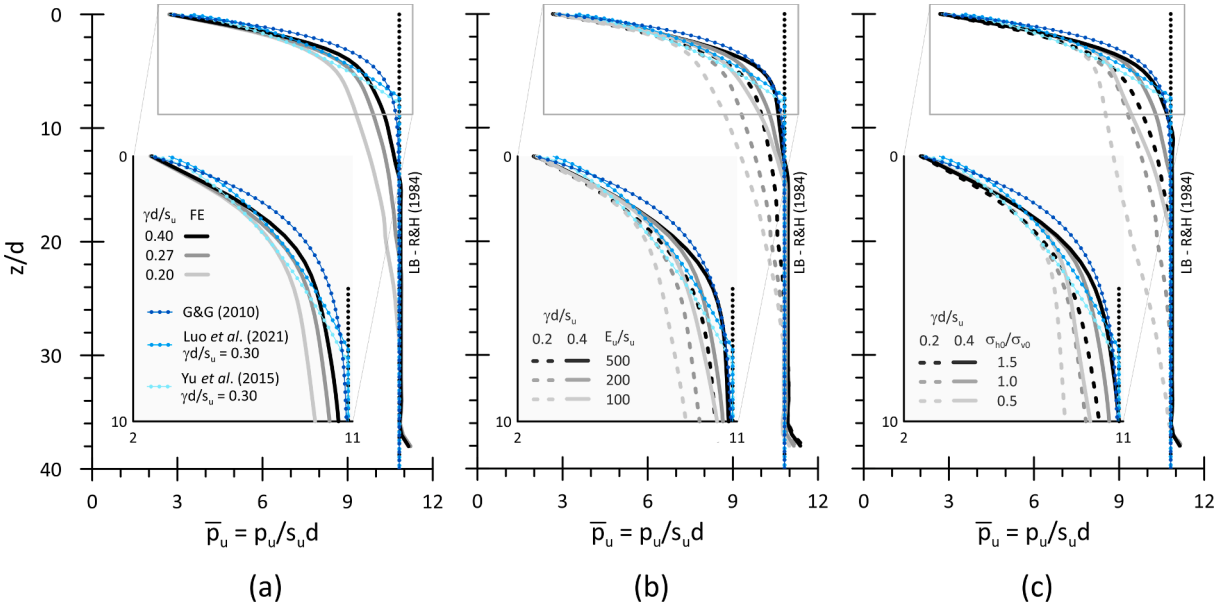

Fig. 8. R-U piles: normalised lateral soil resistance computed for different values of: (a) $\gamma d/s_u$; (b) E_u/s_u; and (c) σ_{h0}/σ_{v0}.

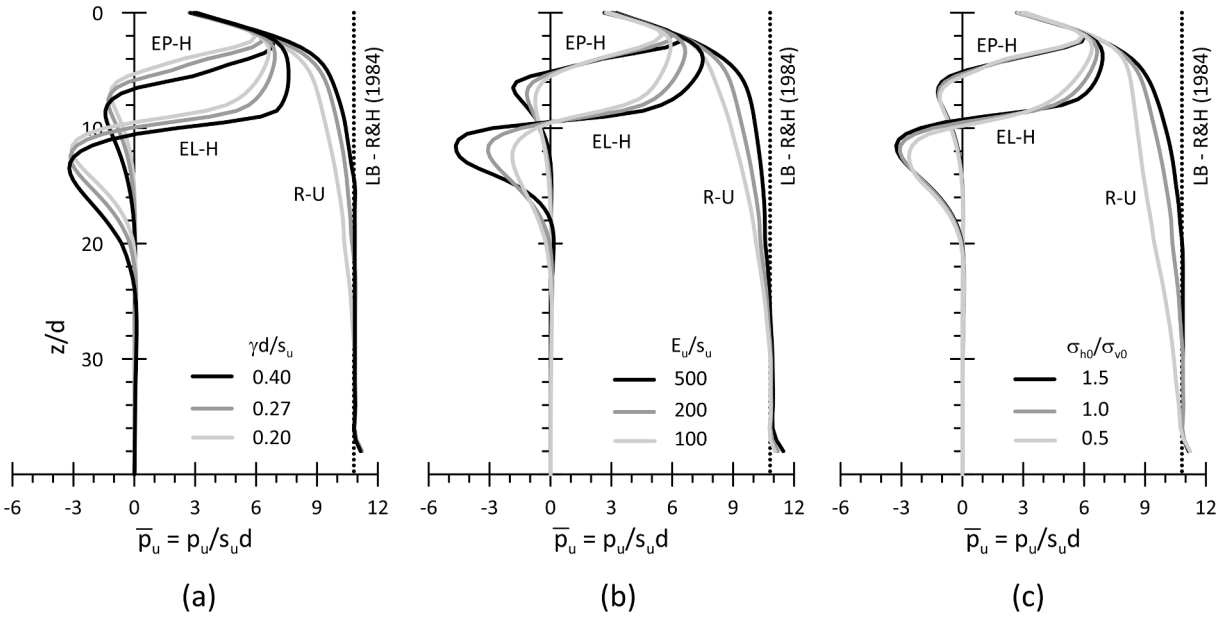

Fig. 9. R-U, free-head EL-H and EP-H piles: normalised lateral soil resistance computed for different values of: (a) $\gamma d/s_u$; (b) E_u/s_u; and (c) σ_{h0}/σ_{v0}.

uniform horizontal displacement (R-U), an increase in the dimensionless ratios $\gamma d/s_u$, E_u/s_u and σ_{h0}/σ_{v0} produces slightly higher contact pressures in the case of the EL-H pile. This effect is quite marginal for the EP-H pile.

4.2. Pile bearing capacity under horizontal loading

A further insight into the behaviour of free-head EL-H and EP-H piles is given in Fig. 10, showing (a) the limiting soil pressure distributions and (b) the normalised horizontal load–displacement curves computed for different $\gamma d/s_u$ values ($E_u/s_u = 200$, $\sigma_{h0}/\sigma_{v0} = 1$, $\alpha = 0.5$). This time, in order to highlight the role of pile diameter on the ultimate response of EP-H piles, variation in the $\gamma d/s_u$ ratio is obtained by changing the pile diameter between 0.5 m and 2.0 m. In the case of elastic EL-H piles, variation of $\gamma d/s_u$ in the range $0.2 \div 0.8$ leads to a significant increase in the maximum normalised contact pressures (+40 %) and horizontal load at the pile head (+20 %). Worth noting here is that an asymptotic behaviour cannot be detected for EL-H piles, at least for an applied horizontal displacement of $u/d = 0.5$, because structural failure cannot occur in this case. As expected, EP-H piles exhibit a completely different response, characterised by the attainment of the lateral capacity for displacements $u/d \approx 0.2$, due to the formation of a plastic hinge within the pile. In this case, the ratio $\gamma d/s_u$ has negligible effects on the contact pressure distribution and, hence, on the pile bearing capacity.

The response of elastoplastic RC piles under free-head (EP-H) and fixed-head (EP-H-fix) conditions is compared in Fig. 11 for three values of E_u/s_u ($\gamma d/s_u = 0.20$; $\sigma_{h0}/\sigma_{v0} = 1$, $\alpha = 0.5$). Specifically, the figure shows: (a) the normalised limit soil resistance distribution; the (b) shear and (c) bending moment distributions along the pile; (d) the normalised horizontal load–displacement curves; and (e) the normalised *N-M*

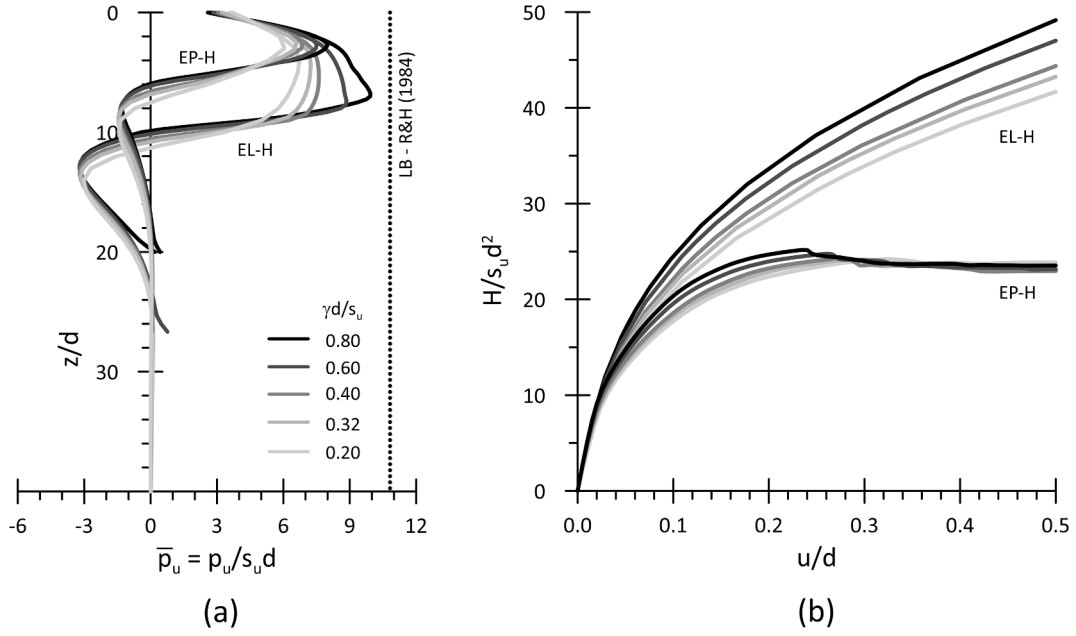

Fig. 10. Free-head EL-H and EP-H piles: (a) soil pressure distributions at failure and (b) normalised load–displacement curves.

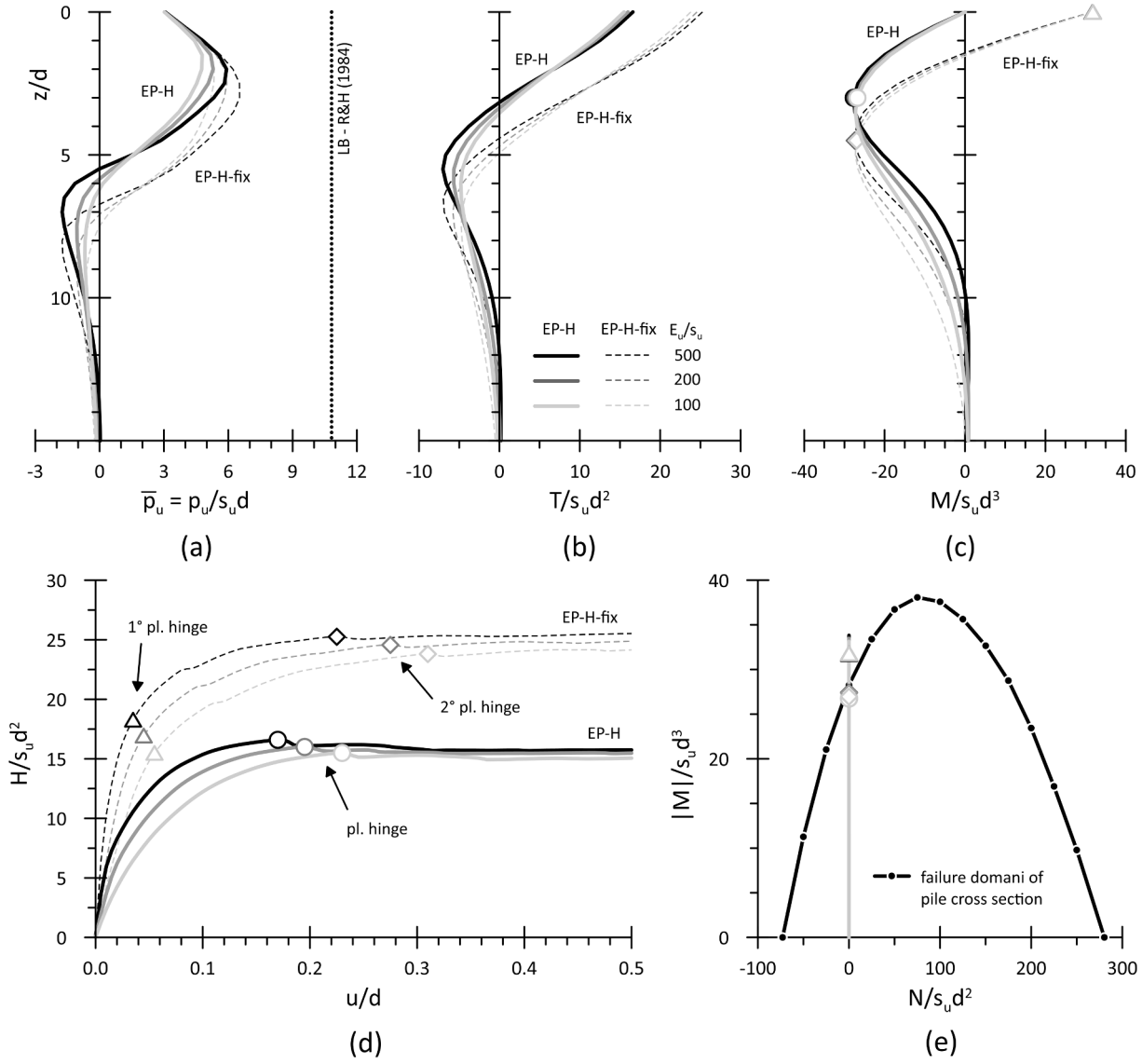

Fig. 11. EP-H and EP-H-fix piles: (a) normalised soil pressure distribution, (b) shear force and (c) bending moment at failure; (d) normalised load–displacement curves; (e) *N-M* interaction diagram and load paths.

interaction diagrams of the pile cross-section, together with the *N-M* load paths computed at the pile cross sections where plastic hinges occurred during the analyses.

Because of the rotational constraint, EP-H-fix piles mobilise higher values of contact pressures with respect to EP-H piles, together with the activation of a deeper failure mechanism (Fig. 11a), leading to an increased lateral capacity (Fig. 11b,d). The typical response of long fixed-head and free-head RC piles is also evident in Fig. 11c, where the bending moment distributions are characterised by two plastic hinges in the first case, one at the head and the other deeper along the shaft, approximately $1 \div 2$ *d* below the plastic hinge developing in the free-head piles. As shown in Fig. 11d,e, the first plastic hinge within the fixed-head piles forms under an applied displacement $u/d \approx 0.05$, while a larger displacement ($u/d \approx 0.25 \div 0.30$) is required to develop the second plastic hinge and to reach the horizontal bearing capacity. Similarly, in free-head piles, the plastic hinge forms at $u/d \approx 0.20$, corresponding to which the pile lateral capacity is attained. As anticipated, the ratio E_u/s_u affects the pile-soil interaction prior to failure, while having negligible influence on the limiting condition of elasto-plastic piles.

Numerical results discussed herein indicate that the horizontal bearing capacity of RC piles is not actually affected by the ratios $\gamma d/s_u$, E_u/s_u and σ_{h0}/σ_{v0}. This result essentially stems from the fact that, due to the formation of plastic hinges along the shaft, the pile response relies on the soil strength mobilised at relatively shallow depths, where the lateral soil resistance basically depends on the adhesion factor, α. Although the sole case of long RC pile was shown, which represent by far the most relevant condition in the design practice, the same conclusions hold for the cases of intermediate and short piles.

5. Simplified theoretical model

Broms' method provides a closed form solution for the undrained horizontal capacity of a single pile in cohesive soils, based on the hypothesis of rigid-plastic behaviour for both the pile and the soil. The assumed limiting soil pressure distribution neglects the contribution given by the soil close to surface ($z < 1.5\ d$), and is characterised by a constant value of $9 s_u d$, regardless of the adhesion factor at the pile-soil interface, thus typically resulting in a conservative estimate of H_u. To overcome such limitation, a more refined limiting distribution is required, but still simple enough to obtain a closed-form expression for H_u.

5.1. Theoretical distribution of limiting soil pressures

Based on FE results discussed in the previous sections, a simple linear distribution was assumed for the limiting contact pressures, taken as a function of the sole adhesion factor, given by:

$$p_u(z) = \begin{cases} p_{u0} + mz & z < z_{lim} \\ p_{u,2D} & z \geq z_{lim} \end{cases} \tag{6}$$

where p_{u0} is the contact pressure at the ground surface and $p_{u,2D}$ is the LB solution by Randolph and Houlsby (1984). Eq. (6) can be written in dimensionless form as:

$$\overline{p}_u(z) = \begin{cases} \overline{p}_{u0} + \overline{m}\overline{z} & \overline{z} < \overline{z}_{lim} \\ \overline{p}_{u,2D} & \overline{z} \geq \overline{z}_{lim} \end{cases} \tag{7}$$

where $\overline{p}_{u0} = p_{u0}/s_u d$, $\overline{m} = m/s_u$ and $\overline{z} = z/d$. Following Georgiadis and Georgiadis (2010) and Luo et al. (2021), a linear relationship was considered between $\overline{p}_{u0}$ and α:

$$\overline{p}_{u0} = 2.35 + 1.25\alpha \tag{8}$$

Eq. (8) is plotted in Fig. 12 together with other numerical and theoretical solutions, indicating a good agreement between the proposed expression and both FE results from this study and the UB solution by Yu et al. (2015). A constant value $\overline{m} = 1.6$, instead, was proven to provide a good match with FE results (see e.g. Fig. 13).

According to Eq. (7), the transition between the wedge and the flow-around mechanism occurs at the limiting normalised depth:

$$\overline{z}_{lim} = \frac{\overline{p}_{u,2D} - \overline{p}_{u0}}{\overline{m}} \tag{9}$$

which varies between 4.2 and 5.2, depending on the adhesion factor. Fig. 13 shows a comparison between the proposed theoretical distribution, FE results and other expressions proposed in the literature, for three values of α (=0, 0.5, 1). Despite its simplicity, Eq. (7) provides a satisfactory representation of the actual limiting soil pressures, both in magnitude and trend.

5.2. Horizontal bearing capacity of free-head and fixed-head piles

Based on the proposed soil resistance distribution, the horizontal pile capacity is reduced to:

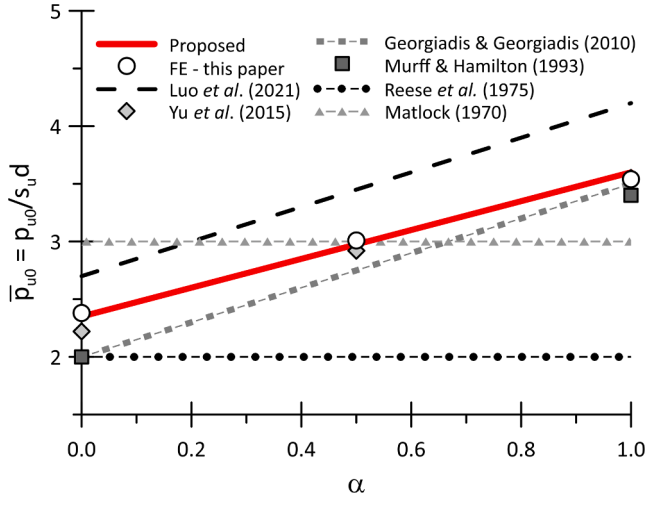

Fig. 12. Variation of the normalised limiting soil resistance at surface, $\overline{p}_{u0}$, with the adhesion factor, α: comparison between FE results and theoretical models. (See above-mentioned reference for further information.)

$$\frac{H_u}{s_u d^2} = F\left(\frac{e}{d}, \frac{L}{d}, \frac{M_{yb}}{s_u d^3}, \frac{p_u(z)}{s_u d}\right) \tag{10}$$

or, equivalently, using Eq. (7):

$$\overline{H}_u = F\left(\overline{e}, \overline{L}, \overline{M}_{yb}, \overline{p}_{u0}, \overline{p}_{u,2D}, \overline{m}\right) \tag{11}$$

where $\overline{H}_u = H_u/s_u d^2$, $\overline{e} = e/d$, $\overline{L} = L/d$, and $\overline{M}_{yb} = M_{yb}/s_u d^3$. The actual dependence of $\overline{H}_u$ on the dimensionless groups in Eq. (11) stems from the restraint at the pile head and the type of structural failure. The following sections provide the closed-form solutions for the free-head and fixed-head pile conditions, all derived under the assumption $\overline{L} \geq \overline{z}_{lim}$, which encompasses all relevant cases in design practice. The corresponding equilibrium equations are detailed in Appendix B.

5.2.1. Free-head pile

As shown in Fig. 14, free-head piles can reach failure following two possible mechanisms: in the first case (short pile), structural yielding does not occur ($M_{max} < M_{yb}$) and the plastic mechanism involves the entire pile length; in the second case (long pile), a plastic hinge develops within the pile, at depth $\overline{f} = f/d$.

Eqs. (12) provide the dimensionless closed-form solutions for the pile lateral capacity and the maximum bending moment, $\overline{M}_{max} = M_{max}/s_u d^3$, for the short pile condition. They exactly define the condition $\overline{f} > \overline{z}_{lim}$ (Fig. 14a), but provide a good approximation also for the case $\overline{f} \leq \overline{z}_{lim}$:

$$\overline{H}_u = \overline{p}_{u,2D}\left[2\sqrt{\left(\frac{\overline{L}^2}{2} + \overline{e}^2 + \overline{L}\overline{e} + \frac{\overline{z}_{lim}^2\overline{m}}{6\overline{p}_{u,2D}}(\overline{z}_{lim} + 3\overline{e})\right)} - \overline{L} - 2\overline{e}\right] - \frac{\overline{z}_{lim}^2\overline{m}}{2} \tag{12a}$$

$$\overline{M}_{max} = \frac{\overline{p}_{u,2D}}{4}\left[\overline{L} - \frac{\overline{H}_u}{\overline{p}_{u,2D}} + \frac{\overline{p}_{u,2D}^2 - \overline{p}_{u0}^2}{2\overline{m}\overline{p}_{u,2D}} - \frac{\overline{p}_{u,2D} - \overline{p}_{u0}}{\overline{m}}\right]^2 \tag{12b}$$

The solution for the long pile condition depends on the position of the plastic hinge. If $\overline{f} \leq \overline{z}_{lim}$ (Fig. 14b), the flow-around mechanism is not mobilised and Eqs. (13) hold:

$$\overline{H}_u = \frac{\overline{p}_{u0}^2}{2\overline{m}}\left[\left(C_1 + C_3\left(1 + \frac{C_3}{C_1}\right)\right)^2 - 1\right] \tag{13a}$$

where

$$C_1 = \left[C_2 + C_3^3 + \sqrt{C_2^2 + 2C_2C_3^3}\right]^{\frac{1}{3}}$$
$$C_2 = \frac{3}{2}\left[\frac{\overline{M}_{yb}\overline{m}^2}{\overline{p}_{u0}^3} - C_3 + \frac{1}{3}\right] \tag{13b}$$
$$C_3 = \frac{1}{2}\left[1 - \frac{\overline{e}\overline{m}}{\overline{p}_{u0}}\right]$$

and:

$$\overline{f} = \frac{\overline{p}_{u0}}{\overline{m}}\left(\sqrt{1 + \frac{2\overline{m}\overline{H}_u}{\overline{p}_{u0}^2}} - 1\right) \tag{13c}$$

If $\overline{f} > \overline{z}_{lim}$ (Fig. 14c), the pile horizontal capacity results from the activation of both the wedge and the plastic flow mechanism. In this case, Eqs. (14) hold:

$$\overline{H}_u = C_1 - \overline{p}_{u,2D}\overline{e} + \overline{p}_{u,2D}\overline{z}_{lim}\left(\sqrt{\left(\frac{\overline{e}}{\overline{z}_{lim}} + 1\right)^2 - 2\frac{(C_1\overline{e} + C_2 - \overline{M}_{yb})}{\overline{p}_{u,2D}\overline{z}_{lim}^2}} - 1\right) \tag{14a}$$

where

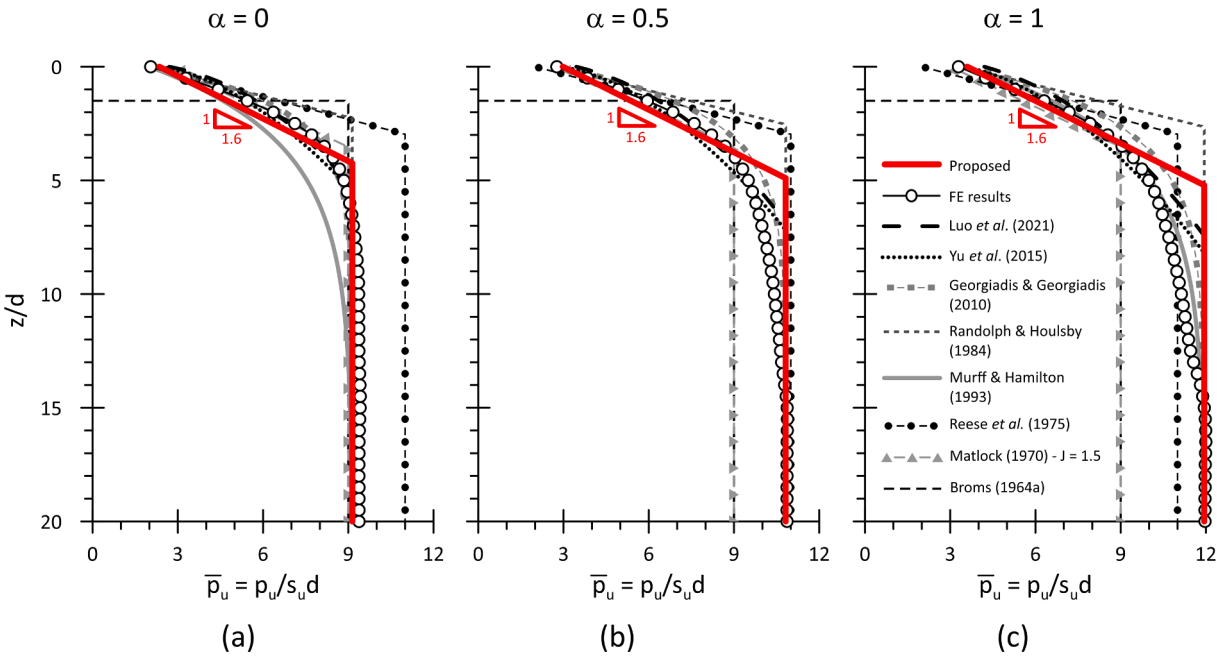

Fig. 13. Theoretical and FE distributions of normalised soil resistance: (a) α = 0; (b) α = 0.5; (c) α = 1 (Analyses # 12, 8, 13 in Tab. 2). (See above-mentioned reference for further information.)

$$C_1 = \frac{(\overline{p}_{u0} + \overline{p}_{u,2D})\overline{z}_{lim}}{2}$$
$$C_2 = \frac{(\overline{p}_{u0} + 2\overline{p}_{u,2D})\overline{z}_{lim}^2}{6} \quad (14b)$$

and

$$\overline{f} = \frac{\overline{H}_u}{\overline{p}_{u,2D}} + \overline{z}_{lim}\left(1 - \frac{\overline{p}_{u0} + \overline{p}_{u,2D}}{2\overline{p}_{u,2D}}\right) \quad (14c)$$

From a practical standpoint, the procedure for calculating $\overline{H}_u$ in the long pile condition can be summarised as follows: (i) compute $\overline{H}_u$ using Eq. (13a); (ii) verify that $\overline{f} \le \overline{z}_{lim}$; (iii) if $\overline{f} > \overline{z}_{lim}$, recalculate $\overline{H}_u$ using Eq. (14a).

5.2.2. *Fixed-head pile*

As shown in Fig. 15, the lateral capacity of fixed-head piles can be achieved either by short, intermediate or long pile failure mechanism.

Eqs. (15) provide the lateral bearing capacity and the maximum bending moment for the short pile condition (Fig. 15a):

$$\overline{H}_u = \frac{(\overline{p}_{u0} + \overline{p}_{u,2D})}{2}\overline{z}_{lim} + \overline{p}_{u,2D}(\overline{L} - \overline{z}_{lim}) \quad (15a)$$

$$\overline{M}_{max} = \frac{(\overline{p}_{u0} + 2\overline{p}_{u,2D})}{6}\overline{z}_{lim}^2 + \overline{p}_{u,2D}\frac{(\overline{L}^2 - \overline{z}_{lim}^2)}{2} \quad (15b)$$

The intermediate pile condition is characterised by the formation of one plastic hinge at the pile head (Fig. 15b). In this case, the plastic mechanism involves the entire pile length and Eq. (16) is the closed-form solution for the problem, while the maximum bending moment along the pile shaft can be computed using Eq. (12b), as the limiting soil pressure distribution coincides with the one mobilised by the free-head short pile (see e.g. Fig. 14a):

$$\overline{H}_u = \overline{p}_{u,2D}\left[2\sqrt{\left(\frac{\overline{M}_{yb}}{\overline{p}_{u,2D}} + \frac{\overline{L}^2}{2} + \frac{\overline{z}_{lim}^3\overline{m}}{6\overline{p}_{u,2D}}\right)} - \overline{L}\right] - \frac{\overline{z}_{lim}^2\overline{m}}{2} \quad (16)$$

The long pile failure mechanism occurs when a second plastic hinge develops at depth $\overline{f}$ along the shaft. If $\overline{f} \le \overline{z}_{lim}$ (Fig. 15c), the pile lateral capacity is given by Eqs. (17), while Eq. (13c) can be used to compute $\overline{f}$, as, once again, the limiting soil pressure distribution coincides with the one mobilised by the corresponding free-head long pile condition (see *e.g.* Fig. 14b):

$$\overline{H}_u = \frac{\overline{p}_{u0}^2}{2\overline{m}}\left[\left(C_1 + \frac{1}{2} + \frac{1}{4C_1}\right)^2 - 1\right] \quad (17a)$$

where:

$$C_1 = \left[\sqrt{C_2^2 - \frac{1}{64}} + C_2\right]^{\frac{1}{3}}$$
$$C_2 = \frac{3\overline{M}_{yb}\overline{m}^2}{\overline{p}_{u0}^3} - \frac{1}{8} \quad (17b)$$

If $\overline{f} > \overline{z}_{lim}$ (Fig. 15d), Eq. (18) provides the closed-form solution for $\overline{H}_u$, while $\overline{f}$ can be computed using Eq. (14c), derived for the corresponding free-head long pile condition (see *e.g.* Fig. 14c):

$$\overline{H}_u = C_1 + \overline{p}_{u,2D}\overline{z}_{lim}\left(\sqrt{1 - 2\frac{(C_2 - 2\overline{M}_{yb})}{\overline{p}_{u,2D}\overline{z}_{lim}^2}} - 1\right) \quad (18)$$

where coefficients C_1 and C_2 are defined by Eq. (14b).

5.3. *Comparison between theoretical solutions and numerical results*

The proposed model was validated against FE analyses of free-head and fixed-head RC piles (d = 1.0 m, d_s/d = 0.9, ρ = 1.8 %), corresponding to which the failure moment of the cross-section is M_{yb} = 2825 kNm for N=0 kN, as indicated by the N-M interaction diagram in Fig. 6c.

In Fig. 16 theoretical predictions are compared with the numerical results of a free-head long pile, computed by varying the soil undrained shear strength within the range 50 ÷ 150 kPa (α = 0.5), in terms of normalised: (a) limiting soil pressure distribution; (b) shear force and (c) bending moment. As expected, an increase in s_u (at constant M_{yb}) leads to a significant reduction of both $\overline{H}_u$ and $\overline{f}$, which is well reproduced by the theoretical model, both in magnitude and trend.

Fig. 17 shows a further comparison between the proposed method

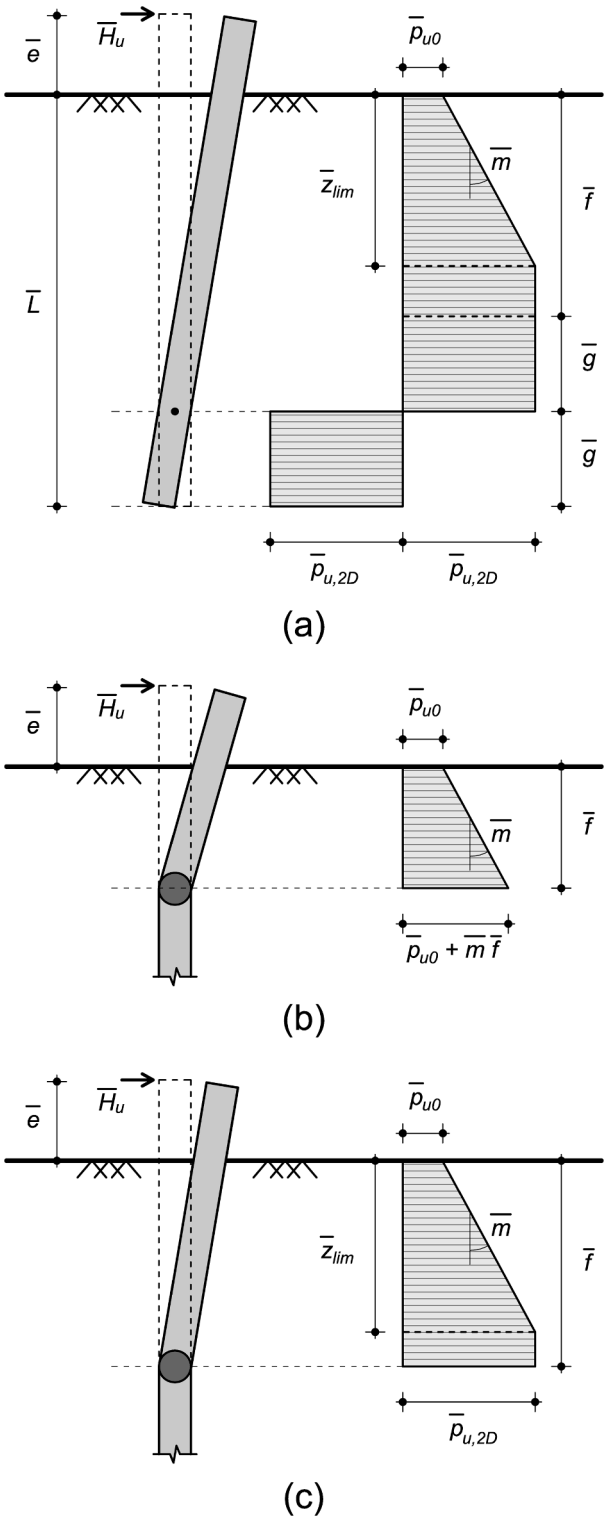

Fig. 14. Free-head pile. Failure mechanism and soil resistance for: (a) short pile; (b) long pile ($\overline{f} \leq \overline{z}_{lim}$); (c) long pile ($\overline{f} > \overline{z}_{lim}$).

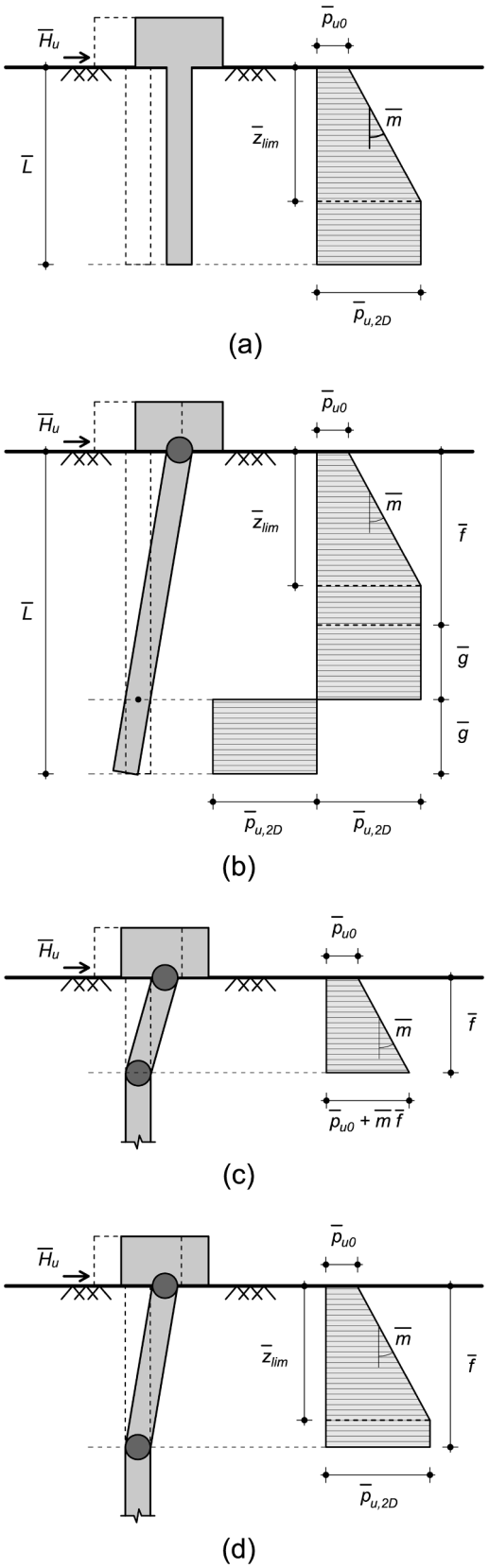

Fig. 15. Fixed-head pile. Failure mechanism and soil resistance for: (a) short pile, (b) intermediate pile; (c) long pile ($\overline{f} \leq \overline{z}_{lim}$); (d) long pile ($\overline{f} > \overline{z}_{lim}$).

and FE results of (a) free-head long piles and (b) fixed-head piles, respectively ($\alpha = 0.5$). This time, FE analyses (#42–56 in Tab. 2) serve as benchmark for validating the theoretical model for different $M_{yb}/s_u d^3$ and e/d (free-head) and $M_{yb}/s_u d^3$ and L/d (fixed-head) ratios. For the sake of completeness, Fig. 17 also displays the $\overline{H}_u$ values provided by classical Broms' solution and those computed by integrating numerically other limiting contact pressure distributions published in the

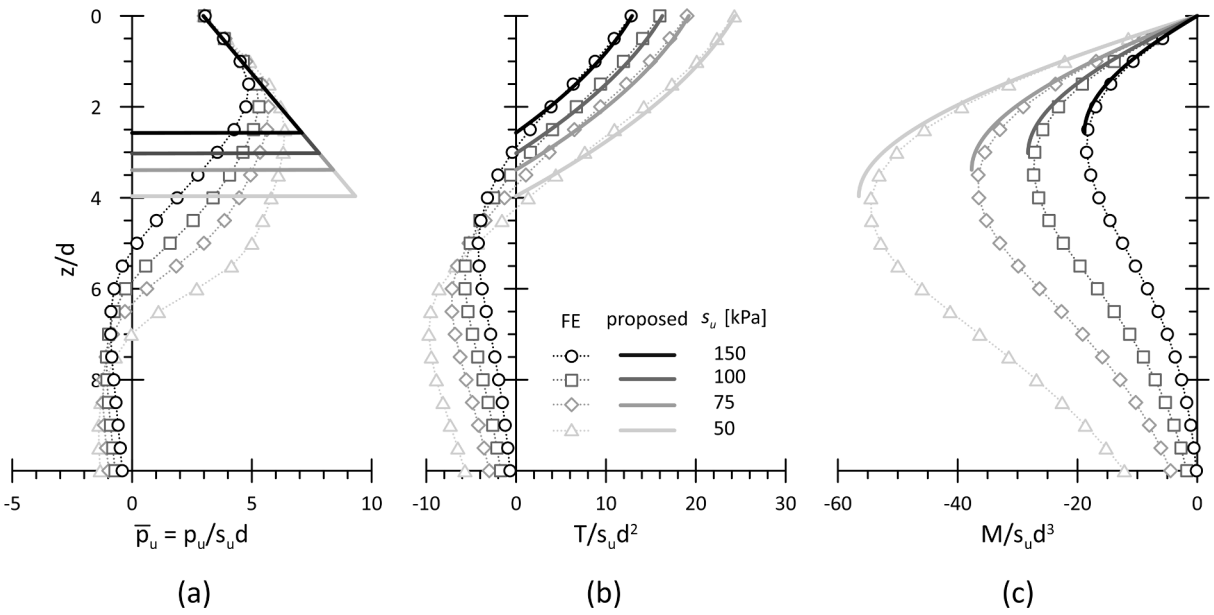

Fig. 16. Free-head long pile: comparison between theoretical and FE results for different values of s_u: (a) soil pressure distribution, (b) shear force and (c) bending moment along the pile.

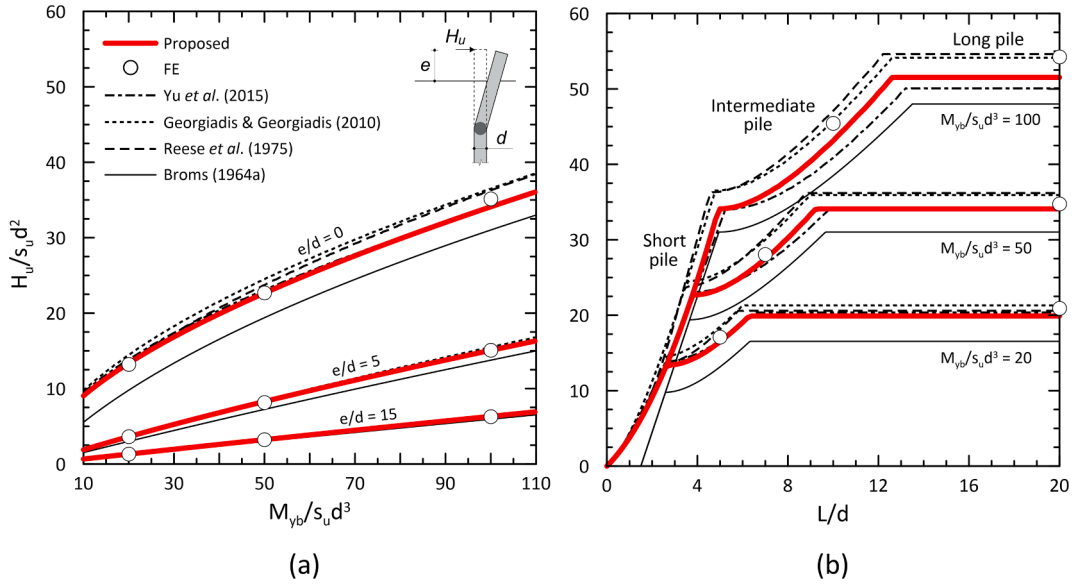

Fig. 17. Dimensionless undrained lateral capacity. Comparison between theoretical solutions and FE results for: (a) free-head long piles and (b) fixed-head piles.

literature (Reese et al., 1975; Georgiadis and Georgiadis, 2010; Yu et al., 2015). The proposed closed-form solution is in good agreement with both FE results and more refined theoretical solutions, providing only slightly conservative results for $M_{yb}/s_u d^3 \geq 100$, in the order of 5 %. As anticipated, instead, Broms' method always predicts smaller values of the horizontal capacity, with maximum differences of about 20 % for both free-head ($M_{yb}/s_u d^3 = 40$) and fixed-head ($L/d = 20$) piles, with respect to the proposed model.

The overall effect of the adhesion factor on the computed $\overline{H}_u$ values is depicted in Fig. 18, showing the theoretical dimensionless charts for: free-head short (a) and long (b) piles ($e/d = 0$, 5, 15); and (c) fixed-head piles ($M_{yb}/s_u d^3 = 10$, 20, 50, 100, 200), the latter exhibiting the typical transition between short, intermediate and long pile failure mechanism. Shaded areas indicate the range of theoretical solutions obtained by varying α between 0 and 1. For the sake of completeness, the theoretical solutions for the cases of short and intermediate piles with $\overline{L} < \overline{z}_{lim}$ are also reported in the figure (dotted curves), obtained by solving iteratively the corresponding equilibrium equations. In the case of free-head piles (Fig. 18a,b), the effect of α on the horizontal pile capacity reduces with increasing the load eccentricity, particularly when a long-pile failure mechanism is activated. For the case of fixed-head piles (Fig. 18c), the effect of α on the computed $\overline{H}_u$ values is marginally dependent on the ratio $M_{yb}/s_u d^3$, with a maximum difference of about 14 % between rough and smooth contact assumption (long pile mechanism).

5.4. Comparison between theoretical solutions and experimental data

With the aim of providing a further validation for the assumed limiting soil pressure distribution, the proposed theoretical model was applied to the analysis of a broad experimental database, consisting of 67 laboratory and field tests on free-head drilled shafts ($2 \leq L/d \leq 10$)

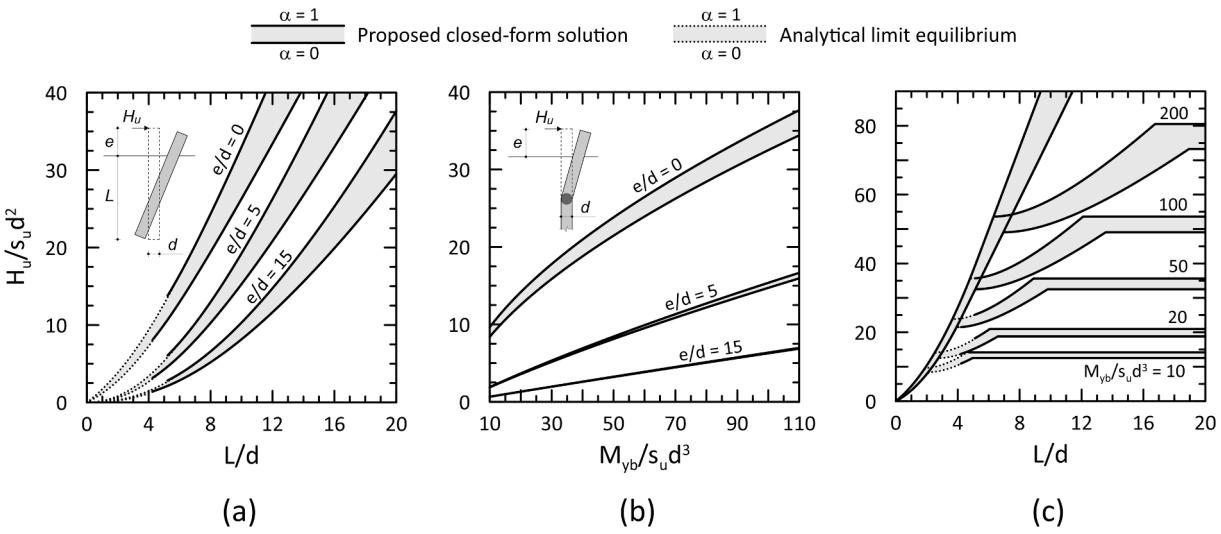

Fig. 18. Theoretical dimensionless charts for the undrained lateral capacity: (a) short and (b) long free-head piles; (c) fixed-head piles.

embedded in clayey soils (Chen and Kulhawy, 1994). Details on the mechanical and physical characterization of soil properties, based on laboratory tests and empirical correlations, were reported by Chen and Kulhawy (1994). Table 3 summarises all relevant geometrical and geotechnical parameters, including: the undrained shear strength in triaxial extension ($s_{u,TE}$) and direct simple shear ($s_{u,DSS}$), appropriate for computing the lateral and tip soil resistance, respectively; the adhesion factor, α, estimated with the empirical equation by Kulhawy (1991); the hyperbolic capacity, $H_{u,hyp}$, computed as the asymptotic limit of the experimental load–displacement curve (Phoon and Kulhawy, 2005; Chen et al., 2011). Following Chen and Kulhawy (1994), all tests were analysed in undrained conditions, assuming a rigid behaviour of the shaft and including the contribution of the tip resistance in the limit equilibrium equations, which can be relevant for small L/d ratios. Fig. 19 shows a comparison between the experimental hyperbolic capacities and the corresponding theoretical limit values computed assuming five different distributions for the lateral soil resistance, while a statistical analysis of all data is reported in Table 4. As expected, with the only exception of Broms' distribution, all models give comparable results, with the mean predicted values included between 71 % (Yu et al. (2015) model) and 92 % (Georgiadis and Georgiadis (2010) model). Once again, despite its simplicity, the proposed theoretical model is in quite good agreement with the experimental data, providing a slightly conservative prediction of the horizontal capacity (mean $H_u/H_{u,hyp} = 82$ %).

5.5. Theoretical failure envelope of laterally loaded piles

As recently discussed by Gerolymos et al. (2020) and Sakellariadis and Anastasopoulos (2024), the horizontal capacity of RC piles, either isolated or within pile groups, strongly depends on the bending moment applied at the pile head, which governs the position of the plastic hinge along the shaft and, hence, the failure mode of the pile. This coupling can be conveniently described through analytical failure envelopes, extending the reference solutions for free-head and fixed-head pile to more general conditions. To this end, the theoretical model illustrated in Sections 5.1 and 5.2 can be easily adapted to describe the ultimate behaviour of a single RC pile under combined *N*–*H*-*M* loading.

By referring to the relevant long pile condition, and after defining the bending moment acting at the pile head as a fraction of the available structural capacity, $M = \beta_y \cdot M_{yb}$ ($-1 \le \beta_y \le 1$), a generalised closed form solution for the normalised bearing capacity, $\overline{H}_u$, can be derived from the equilibrium equations of the pile. Specifically, for $\overline{f} \le \overline{z}_{lim}$, $\overline{H}_u$ is given by:

$$\overline{H}_u = \frac{\overline{p}_{u0}^2}{2\overline{m}}\left[\left(C_1 + \frac{1}{2} + \frac{1}{4C_1}\right)^2 - 1\right] \tag{19a}$$

$$C_1 = \left[\sqrt{C_2^2 - \frac{1}{64}} + C_2\right]^{\frac{1}{3}}$$
$$C_2 = \frac{3(1-\beta_y)\overline{M}_{yb}\overline{m}^2}{2\overline{p}_{u0}^3} - \frac{1}{8} \tag{19b}$$

while, for $\overline{f} > \overline{z}_{lim}$, it is:

$$\overline{H}_u = C_1 + \overline{p}_{u,2D}\overline{z}_{lim}\left(\sqrt{1 - 2\frac{C_2 - (1-\beta_y)\overline{M}_{yb}}{\overline{p}_{u,2D}\overline{z}_{lim}^2}} - 1\right) \tag{20a}$$

$$C_1 = \frac{(\overline{p}_{u0} + \overline{p}_{u,2D})\overline{z}_{lim}}{2}$$
$$C_2 = \frac{(\overline{p}_{u0} + 2\overline{p}_{u,2D})\overline{z}_{lim}^2}{6} \tag{20b}$$

The condition $\beta_y = -1$ corresponds to the classical fixed-head failure mode. With increasing β_y, the plastic hinge at depth tends to develop closer and closer to the pile head ($\overline{f} \to 0$), with a concurrent reduction of $\overline{H}_u$. At the limiting condition $\beta_y = 1$, when $M = M_{yb}$ at the pile head, the two plastic hinges collapse into one and $\overline{H}_u = 0$.

Numerical and theoretical *H*-*M* interaction diagrams are compared in Fig. 20b for the case of a single pile ($d = 1$ m, $\rho = 1.8$ %, $L/d = 15$, $\alpha = 0.5$, $\gamma d/s_u = 0.2$, $E_u/s_u = 200$, $\sigma_{h0}/\sigma_{v0} = 1$) subjected to three different values of the axial load (N=1.58 MN, 0 MN, −1.13 MN), comprised between the axial bearing capacity in compression and uplift. For the sake of completeness, Fig. 20a displays also the *N*-*M* failure domain of the pile cross-section. Moreover, theoretical *H*-*M* domains are computed using both the proposed model (Eqs.(19) and (20)) and the closed-form solution provided by Gerolymos et al. (2020), which assumes a constant distribution of the lateral soil pressures, $p_{u0} = 10 s_u d$, up to the soil surface. As expected, due to the *N*-*M* structural coupling, the *H*-*M* domain expands with increasing the axial load at the pile head. Furthermore, a positive bending moment reduces the horizontal capacity, up to the limit case where $M = M_{yb}$ and $H_u = 0$. A beneficial effect is induced, instead, by a negative bending moment, with the limiting condition $M = -M_{yb}$ for the fixed-head pile mechanism. As apparent, the proposed solution describes accurately the interaction between H_u and the *N*-*M* loads applied at the pile head. Quite the opposite, the theoretical model proposed by Gerolymos et al. (2020) leads to

Table 3
Laboratory and field tests on free-head drilled shafts in clayey soils: relevant geometrical and geotechnical parameters (modified after Chen and Kulhawy, 1994). (*Units: [N] for laboratory tests and [kN] for field tests).

type	L	d	e	$s_{u,TE}$	$s_{u,DSS}$	$H_{u,hyp}$	γ	α	$H_u/H_{u,hyp}$				
	m	m	m	kPa	kPa	(*)	kN/m^3	–	Broms	Reese *et al.*	G&G	Yu *et al.*	Proposed
lab	0.300	0.089	0.315	3.56	5.9	113	18.0	1	0.37	0.80	0.92	0.70	0.81
lab	0.300	0.089	0.315	3.56	5.9	135	18.0	1	0.31	0.67	0.77	0.59	0.68
lab	0.300	0.089	0.02	2.07	3.4	225	17.8	1	0.23	0.52	0.61	0.47	0.53
lab	0.300	0.089	0.02	2.07	3.4	237	17.8	1	0.22	0.50	0.57	0.45	0.50
lab	0.533	0.089	0.025	2.42	4.1	454	18.1	1	0.46	0.70	0.74	0.56	0.67
lab	0.533	0.089	0.025	3.45	5.7	667	18.6	1	0.45	0.68	0.72	0.54	0.65
lab	0.533	0.089	0.025	3.45	5.7	556	18.6	1	0.54	0.81	0.86	0.65	0.78
lab	0.355	0.089	0.025	1.75	2.9	167	18.0	1	0.40	0.76	0.85	0.66	0.74
lab	0.355	0.089	0.025	1.75	2.9	155	18.0	1	0.43	0.82	0.91	0.71	0.80
lab	0.355	0.089	0.025	3.12	5.1	266	18.5	1	0.45	0.83	0.95	0.72	0.83
lab	0.355	0.089	0.025	3.12	5.1	245	18.5	1	0.48	0.90	1.03	0.78	0.90
lab	0.267	0.089	0.02	4.21	6.9	379	18.7	1	0.20	0.51	0.62	0.48	0.54
lab	0.267	0.089	0.02	4.21	6.9	335	18.7	1	0.23	0.58	0.71	0.54	0.62
lab	0.710	0.089	0.02	5.26	8.8	1101	18.8	1	0.68	0.93	0.98	0.72	0.90
lab	0.710	0.089	0.02	5.26	8.8	1357	18.8	1	0.55	0.76	0.79	0.59	0.73
lab	0.267	0.089	0.279	1.62	2.7	29	17.6	1	0.48	1.24	1.42	1.14	1.25
lab	0.267	0.089	0.279	1.62	2.7	30	17.6	1	0.47	1.20	1.37	1.10	1.21
lab	0.355	0.089	0.02	1.75	2.9	143	18.1	1	0.47	0.91	1.00	0.79	0.88
lab	0.355	0.089	0.02	1.75	2.9	177	18.1	1	0.38	0.74	0.81	0.64	0.71
lab	0.533	0.089	0.02	4.87	8.1	1120	18.6	1	0.38	0.57	0.61	0.45	0.55
lab	0.533	0.089	0.02	4.87	8.1	805	18.6	1	0.53	0.79	0.85	0.63	0.77
lab	0.355	0.089	0.035	4.47	7.3	580	18.7	1	0.28	0.53	0.60	0.45	0.53
lab	0.355	0.089	0.02	2.17	3.6	253	18.1	1	0.33	0.63	0.70	0.54	0.62
lab	0.355	0.089	0.38	2.18	3.6	113	18.1	1	0.33	0.62	0.68	0.53	0.60
lab	0.355	0.089	0.38	2.18	3.6	99	18.1	1	0.38	0.71	0.78	0.60	0.69
lab	0.533	0.089	0.025	7.06	11.8	1350	18.9	1	0.45	0.67	0.73	0.53	0.66
lab	0.533	0.089	0.025	6.44	10.8	1048	18.9	1	0.53	0.79	0.86	0.63	0.77
lab	0.267	0.089	0.025	3.5	5.7	136	18.1	1	0.46	1.17	1.41	1.08	1.23
lab	0.267	0.089	0.025	3.5	5.7	123	18.1	1	0.50	1.30	1.56	1.19	1.36
lab	0.267	0.089	0.025	2.02	3.3	135	17.8	1	0.27	0.70	0.82	0.65	0.72
lab	0.267	0.089	0.025	2.02	3.3	126	17.8	1	0.28	0.75	0.88	0.69	0.77
lab	0.533	0.089	0.03	4.1	6.8	436	18.3	1	0.81	1.21	1.29	0.96	1.17
lab	0.533	0.089	0.03	4.1	6.8	550	18.3	1	0.64	0.96	1.03	0.76	0.93
lab	0.533	0.089	0.03	2.39	4.1	331	17.9	1	0.62	0.94	1.00	0.75	0.90
lab	0.533	0.089	0.03	2.39	4.1	375	17.9	1	0.55	0.83	0.88	0.66	0.79
lab	1.050	0.175	0.05	4.9	8.3	3450	18.6	1	0.48	0.73	0.77	0.58	0.69
lab	1.050	0.175	0.05	4.9	8.3	3707	18.6	1	0.45	0.68	0.71	0.54	0.64
lab	0.305	0.051	0.025	3.63	5.9	347	18.6	1	0.28	0.42	0.46	0.33	0.41
lab	0.305	0.051	0.025	3.63	5.9	222	18.6	1	0.44	0.66	0.71	0.52	0.64
lab	0.533	0.089	2.132	2.41	4.1	70	17.9	1	0.47	0.71	0.74	0.57	0.69
lab	0.533	0.089	2.131	2.41	4.1	75	17.9	1	0.44	0.66	0.69	0.53	0.65
lab	0.533	0.089	0.533	2.42	4.1	266	18.1	1	0.35	0.53	0.56	0.42	0.52
lab	0.533	0.089	0.533	2.42	4.1	272	18.1	1	0.34	0.51	0.55	0.41	0.50
lab	0.267	0.089	1.07	2.02	3.3	12	17.7	1	0.53	1.37	1.57	1.22	1.39
lab	0.267	0.089	1.07	2.02	3.3	16	17.7	1	0.40	1.03	1.18	0.92	1.04
lab	0.267	0.089	0.267	2.02	3.3	63	17.7	1	0.28	0.73	0.84	0.66	0.74
lab	0.267	0.089	0.267	2.02	3.3	64	17.7	1	0.28	0.72	0.82	0.78	0.73
field	6.1	0.91	0.79	44	63	882	19.7	0.80	0.49	0.71	0.73	0.56	0.66
field	4.57	0.91	0.79	45	63	634	20	0.79	0.40	0.64	0.69	0.52	0.60
field	4.57	0.76	0.79	45	63	486	20	0.79	0.50	0.75	0.79	0.60	0.70
field	2.44	0.81	7.44	30	45	45	20.5	1.00	0.23	0.57	0.65	0.50	0.56
field	3.66	0.81	7.44	30	45	68	20.5	1.00	0.52	0.89	0.97	0.74	0.87
field	2.44	0.81	7.35	7	6	8.7	15.7	1.00	0.26	0.70	0.76	0.63	0.68
field	3.66	0.81	7.38	8	9	33	15.7	1.00	0.28	0.50	0.53	0.42	0.48
field	3.57	1.37	24.38	58	108	115	20.2	0.66	0.15	0.48	0.55	0.44	0.46
field	3.81	1.52	24.38	62	205	176	21	0.63	0.13	0.44	0.50	0.42	0.44
field	6.17	1.98	24.38	46	47	124	22	0.78	0.63	1.60	1.68	1.40	1.44
field	5.33	1.37	24.38	36	69	143	18.2	0.93	0.34	0.64	0.69	0.53	0.60
field	4.57	1.37	24.38	35	75	166	17.5	0.95	0.18	0.37	0.41	0.33	0.36
field	11	1.83	0.28	55	122	2390	20.4	0.68	0.86	1.32	1.33	1.06	1.17
field	1.83	0.61	3.05	30	67	17	19.8	1.00	0.57	1.35	1.59	1.23	1.40
field	1.37	0.61	3.05	30	67	13	19.8	1.00	0.22	0.96	1.21	0.95	1.07
field	6.4	0.61	0.46	55	75	883	20	0.68	0.57	0.76	0.76	0.59	0.70
field	10	1	2.25	11	16	126	15.7	1.00	1.70	2.35	2.36	1.87	2.22
field	10	1	2.25	11	16	123	15.7	1.00	1.75	2.40	2.42	1.92	2.27
field	4.4	0.95	2.2	14	20	115	15.5	1.00	0.47	0.80	0.88	0.68	0.78
field	5.2	0.67	0.67	98	257	893	21	0.48	0.74	1.02	1.00	0.79	0.90

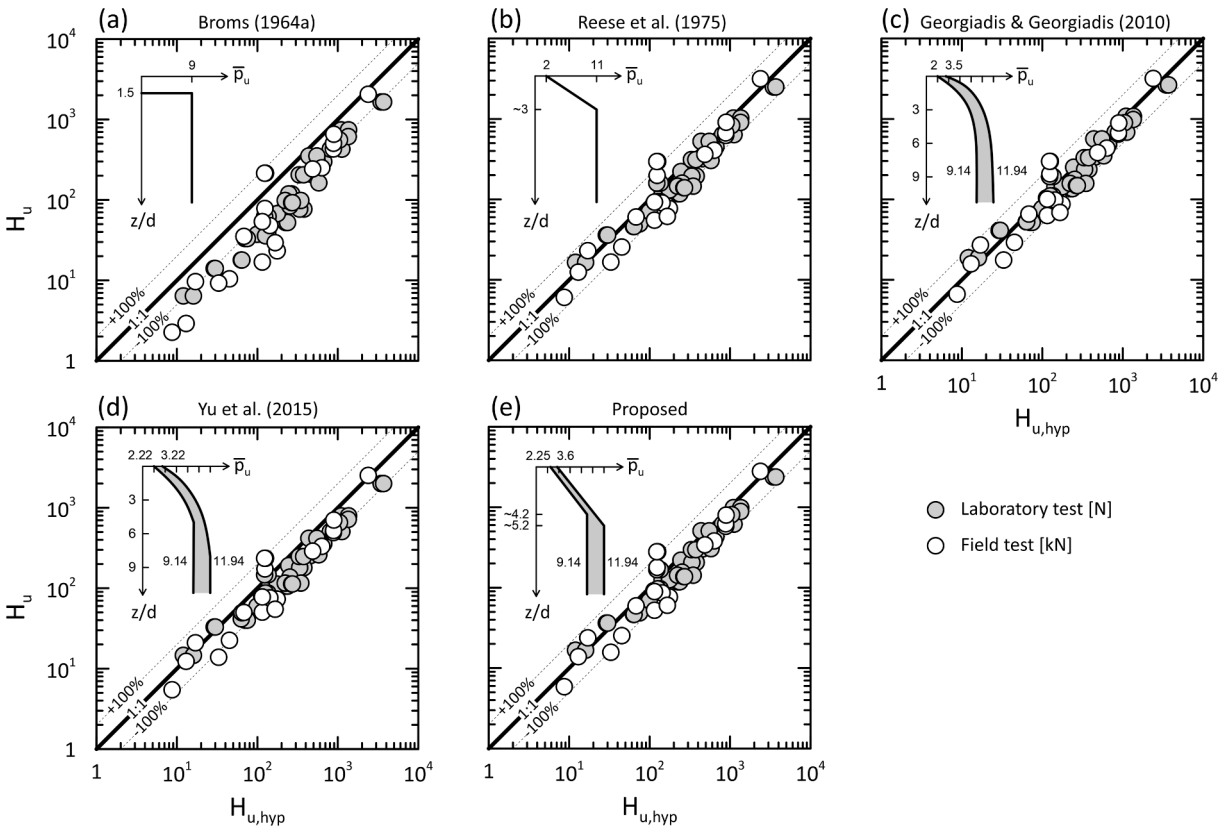

Fig. 19. Comparison between measured and predicted lateral capacities of rigid drilled shafts in cohesive soils, using the theoretical distributions proposed by: (a) Broms (1964a); (b) Reese et al. (1975); (c) Georgiadis and Georgiadis (2010); (d) Yu et al., (2015); (e) this work.

Table 4
Undrained lateral load tests on free-head drilled shafts in clayey soils: summary of regression analysis for different theoretical soil pressure distributions.

	$H_u/H_{u,hyp}$				
	Broms (1964a)	Reese et al. (1975)	G&G (2010)	Yu et al. (2015)	Proposed
# of tests	67	67	67	67	67
mean	0.46	0.84	0.92	0.71	0.82
dev. st.	0.27	0.37	0.39	0.31	0.35

unconservative predictions of the ultimate domain, essentially due to the high limiting soil pressure assumed close to the soil surface.

A further insight into the behaviour of a single pile under generalised loads is given in Fig. 21, where FE results referring to three values of the applied bending moment (β_y = 0.9, 0, −1 at N=0 MN) are compared with the proposed model predictions, in terms of: (a) limiting soil pressure distributions, (b) shear force and (c) bending moment along the pile. Fig. 21d also displays the contours of axial deformations within the pile, highlighting the actual failure mode corresponding to each applied load.

Clearly, the moment applied at the pile head does not affect the limiting soil pressure distribution ($\overline{p}_{u0}$ and $\overline{m}$), which depends only on the adhesion factor, but rather the position of the plastic hinge at depth, which in turn affects both the pile horizontal capacity and the structural internal forces. This behaviour is well reproduced by the proposed theoretical model, which turns out to be in very good agreement with FE results.

6. Conclusions

This paper presented the main results of a numerical and theoretical study on the undrained lateral capacity of RC piles in cohesive soils. 3D FE analyses were carried out by adopting suitable constitutive assumptions for both materials and interfaces. Among these, the CDP model was used to reproduce the highly nonlinear behaviour of concrete in tension and compression, which is an essential ingredient when modelling the ultimate response of piles under lateral loading.

Numerical analyses confirmed that the horizontal bearing capacity of piles is strongly affected by the mutual interplay between the wedge and flow-around plastic mechanisms occurring in the adjacent soil. However, based on the results of an extensive parametric study, it was shown that, contrary to what observed for rigid and elastic piles, dimensionless ratios E_u/s_u, $\gamma d/s_u$ and σ_{h0}/σ_{v0} have a negligible influence on the ultimate response of RC piles, which essentially depends on the adhesion factor, α.

Based on numerical outcomes, a new theoretical distribution was proposed for the limiting lateral soil resistance, simple enough to derive closed-form solutions for the undrained lateral capacity of free-head and fixed-head piles, considering all possible failure modes.

The proposed model was validated against both numerical FE results of RC piles and experimental data of rigid shafts embedded in cohesive soils. It allowed overcoming inherent conservativeness of classical Broms's theory, providing results in very good agreement with those obtained by integrating numerically more refined limiting soil pressure distributions. Due to its simplicity, this model was easily adapted to derive the theoretical failure domain of a single long pile under generalised N–H–M loading, extending the classical solutions for free-head and fixed-head pile to more general failure conditions. The proposed solutions can be readily used in the design of single piles, as well as in the computation of three-dimensional interaction domains of pile groups and piled-rafts.

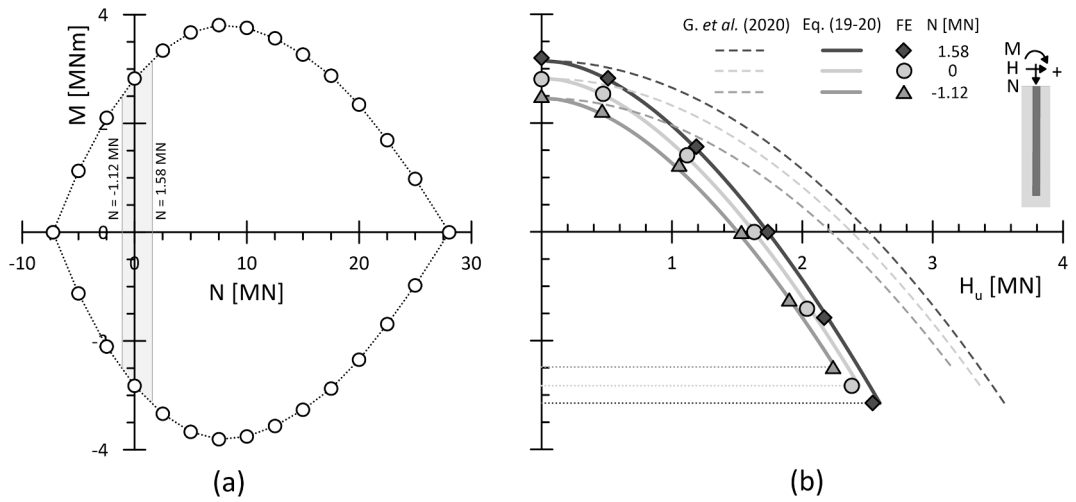

Fig. 20. Single pile subject to combined N–H-M loading: (a) N-M failure domain of the pile cross-section; (b) comparison between numerical and theoretical H-M failure envelopes computed at three values of the applied axial load, N=1.58 MN, 0 MN, −1.13 MN ($d = 1$ m, $\rho = 1.8$ %, $L/d = 15$, $\alpha = 0.5$, $\gamma d/s_u = 0.2$, $E_u/s_u = 200$, $\sigma_{h0}/\sigma_{v0} = 1$).

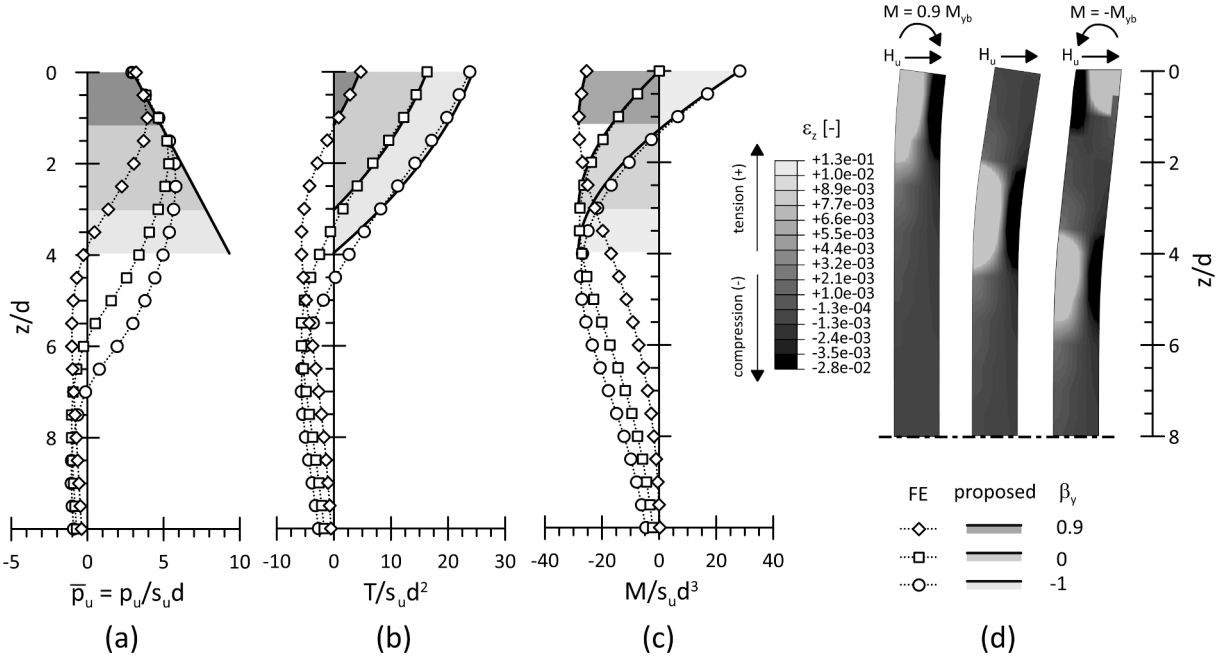

Fig. 21. Single pile subject to combined N–H-M loading (by = 0.9, 0, −1; N=0 kN). Comparison between numerical and theoretical distributions of (a) limiting soil pressures, (b) shear force and (c) bending moment along the pile; (d) contours of axial deformations within the pile ($d = 1$ m, $\rho = 1.8$ %, $L/d = 15$, $\alpha = 0.5$, $\gamma d/s_u = 0.2$, $E_u/s_u = 200$, $\sigma_{h0}/\sigma_{v0} = 1$).

CRediT authorship contribution statement

Francesco Potini: Writing – review & editing, Writing – original draft, Validation, Software, Methodology, Conceptualization. **Riccardo Conti:** Writing – review & editing, Writing – original draft, Validation, Supervision, Methodology, Funding acquisition, Conceptualization.

Declaration of competing interest

The authors declare the following financial interests/personal relationships which may be considered as potential competing interests: Francesco Potini reports financial support was provided by Lazio Region and Italferr S.p.A.. If there are other authors, they declare that they have no known competing financial interests or personal relationships that could have appeared to influence the work reported in this paper.

Data availability

Data will be made available on request.

Acknowledgments

Financial support for this research was provided by Regione Lazio (Italy) and Italferr S.p.A. within the programme POR-FSE 2014-2020 (Grant Agreement no. F83C22000770005). The Authors wish to acknowledge dr. Letizia Berardi, dr. Andrea F. Rotunno and prof. Giulia Viggiani for many fruitful discussions during the initial stages of the work. The Authors are also extremely grateful to the anonymous Reviewers, whose comments and suggestions led to a significant improvement of the manuscript.

Appendix A

In this section, the evolution equations and assumptions of the rate-independent CDP model available in ABAQUS (Abaqus, 2017) are briefly recalled. The sign convention usually adopted in solid mechanics (tensile stresses positive) is adopted throughout; moreover, following standard notation, bold-face letters denote vectors and second-order tensors, while blackboard-bold symbols denote fourth-order tensors.

Disregarding the elastic stiffness degradation due to damage evolution, which was not implemented in the present work, the elastoplastic evolution problem can be summarised as follows:

(i) Strain rates are decomposed into an elastic, $\dot{\boldsymbol{\varepsilon}}^e$, and plastic part, $\dot{\boldsymbol{\varepsilon}}^p$, as:

$$\dot{\boldsymbol{\varepsilon}} = \dot{\boldsymbol{\varepsilon}}^e + \dot{\boldsymbol{\varepsilon}}^p \tag{A1}$$

(ii) The rate form of the constitutive equation is given by:

$$\dot{\boldsymbol{\sigma}} = \mathbb{C}(\dot{\boldsymbol{\varepsilon}} - \dot{\boldsymbol{\varepsilon}}^p) \tag{A2}$$

where $\mathbb{C}$ is the fourth-order elastic stiffness tensor.

(iii) The evolution of plastic strains is defined by a non-associated flow rule:

$$\dot{\boldsymbol{\varepsilon}}^p = \dot{\lambda}\frac{\partial G(\boldsymbol{\sigma})}{\partial \boldsymbol{\sigma}} \tag{A3}$$

where $G(\boldsymbol{\sigma})$ is the plastic potential and $\dot{\lambda}$ is the plastic multiplier.

(iv) damage states associated to cracking (in tension) and crushing (in compression) are described through two internal scalar variables, $\tilde{\varepsilon}_t^p$ and $\tilde{\varepsilon}_c^p$, defined as the effective plastic strain in tension and compression, respectively. Hence, the hardening law is given by:

$$\dot{\tilde{\boldsymbol{\varepsilon}}}^p = \boldsymbol{h}(\boldsymbol{\sigma}, \tilde{\boldsymbol{\varepsilon}}^p)\dot{\hat{\boldsymbol{\varepsilon}}}^p \tag{A4}$$

where $\boldsymbol{h}(\boldsymbol{\sigma}, \tilde{\boldsymbol{\varepsilon}}^p)$ is a suitable hardening function; $\tilde{\boldsymbol{\varepsilon}}^p = \left[\tilde{\varepsilon}_t^p, \tilde{\varepsilon}_c^p\right]$ is the vector of effective plastic strains; and $\dot{\hat{\boldsymbol{\varepsilon}}}^p = \left[\dot{\hat{\varepsilon}}_1^p, \dot{\hat{\varepsilon}}_2^p, \dot{\hat{\varepsilon}}_3^p\right]$, where $\dot{\hat{\varepsilon}}_1^p \geq \dot{\hat{\varepsilon}}_2^p \geq \dot{\hat{\varepsilon}}_3^p$ are the eigenvalues of the plastic strain rate tensor.

(v) Admissible stress states are constrained by the following condition:

$$F(\boldsymbol{\sigma}, f_t, f_c) \leq 0 \tag{A5}$$

where $F(\boldsymbol{\sigma}, f_t, f_c)$ is the yield function, while f_t and f_c are the uniaxial strength of the material in tension and compression, respectively, which evolve with increasing the effective plastic strains.

(vi) The plastic multiplier and the yield function must obey the Kuhn-Tucker and the consistency conditions:

$$\dot{\lambda} \geq 0, F \leq 0, \dot{\lambda}F = 0, \dot{\lambda}\dot{F} = 0 \tag{A6}$$

The evolution of the yield function in the plastic regime is formulated under uniaxial loading and then extended to multiaxial conditions. In the former case, it is assumed that $\dot{\tilde{\boldsymbol{\varepsilon}}}^p$ is given by

$$\begin{aligned} \dot{\tilde{\varepsilon}}_t^p &= \dot{\varepsilon}_1^p (\text{uniaxial tension}) \\ \dot{\tilde{\varepsilon}}_c^p &= -\dot{\varepsilon}_1^p (\text{uniaxial compression}) \end{aligned} \tag{A7}$$

and that the uniaxial stress–strain curves can be converted into uniaxial strength versus effective plastic strain curves (see e.g. Fig. A1), in the form:

$$\begin{aligned} f_t &= f_t\left(\tilde{\varepsilon}_t^p\right) \\ f_c &= f_c\left(\tilde{\varepsilon}_c^p\right) \end{aligned} \tag{A8}$$

Under multiaxial conditions, the hardening function is defined as:

$$\boldsymbol{h}(\boldsymbol{\sigma}, \tilde{\boldsymbol{\varepsilon}}^p) = \begin{bmatrix} r(\hat{\boldsymbol{\sigma}}) & 0 & 0 \\ 0 & 0 & -(1 - r(\hat{\boldsymbol{\sigma}})) \end{bmatrix} \tag{A9}$$

where $0 \leq r(\hat{\boldsymbol{\sigma}}) \leq 1$ is a stress weight factor:

$$r(\hat{\boldsymbol{\sigma}}) = \frac{\sum_{i=1}^{3} \langle \hat{\sigma}_i \rangle}{\sum_{i=1}^{3} |\hat{\sigma}_i|} \tag{A10}$$

where $\hat{\sigma}_i$ are the pricipal stresses and $\langle \bullet \rangle$ are the Macauley brackets, defined by $\langle x \rangle = \frac{1}{2}(x + |x|)$.

The yield function is defined as:

$$F(\boldsymbol{\sigma}, f_t, f_c) = \frac{1}{1-\alpha}[q - 3\alpha \bullet p + \beta(\tilde{\boldsymbol{\varepsilon}}^p)\langle \hat{\sigma}_{\max} \rangle - \gamma\langle -\hat{\sigma}_{\max} \rangle] - f_c\left(\tilde{\varepsilon}_c^p\right) \leq 0 \tag{A11}$$

where

$$p = -\frac{1}{3}\mathrm{tr}(\boldsymbol{\sigma}); \quad q = \sqrt{\frac{3}{2}}\|\boldsymbol{S}\|; \quad \boldsymbol{S} = \boldsymbol{\sigma} - \frac{1}{3}\mathrm{tr}(\boldsymbol{\sigma})\boldsymbol{I}; \quad \widehat{\sigma}_{\max} = \max_i \widehat{\sigma}_i$$

and $\beta(\tilde{\boldsymbol{\varepsilon}}^p)$ is given by:

$$\beta(\tilde{\boldsymbol{\varepsilon}}^p) = \frac{f_c\left(\tilde{\varepsilon}_c^p\right)}{f_t\left(\tilde{\varepsilon}_t^p\right)}(1-\alpha) - (1+\alpha) \tag{A12}$$

The dimensionless parameters α and γ determine the shape of the yield function in biaxial compression ($\widehat{\sigma}_{\max} = 0$) and triaxial compression ($\widehat{\sigma}_{\max} < 0$), respectively, corresponding to which they are defined as:

$$\alpha = \frac{f_{b0}/f_{c0} - 1}{2f_{b0}/f_{c0} - 1} \tag{A13}$$

and

$$\gamma = \frac{3(1-K_c)}{2K_c - 1} \tag{A14}$$

where $K_c = q_{\mathrm{TM}}/q_{\mathrm{CM}}$, with q_{TM} and q_{CM} being the yielding deviatoric stresses along the tensile meridian (TM) and compressive meridian (CM). Typical values for concrete are $K_c = 2/3$ and $f_{\mathrm{b0}}/f_{\mathrm{c0}} = 1.16$ (Lubliner et al., 1989).

Finally, the plastic potential is given by the classical Drucker-Prager hyperbolic function:

$$G(\boldsymbol{\sigma}) = \sqrt{\left(\varepsilon f_{t0}\tan\psi\right)^2 + q^2} - p\tan\psi \tag{A15}$$

where ψ is the dilatancy angle, f_{t0} is the uniaxial tensile yield stress and ε is the eccentricity parameter, controlling the rate at which the hyperbolic function approaches the asymptote.

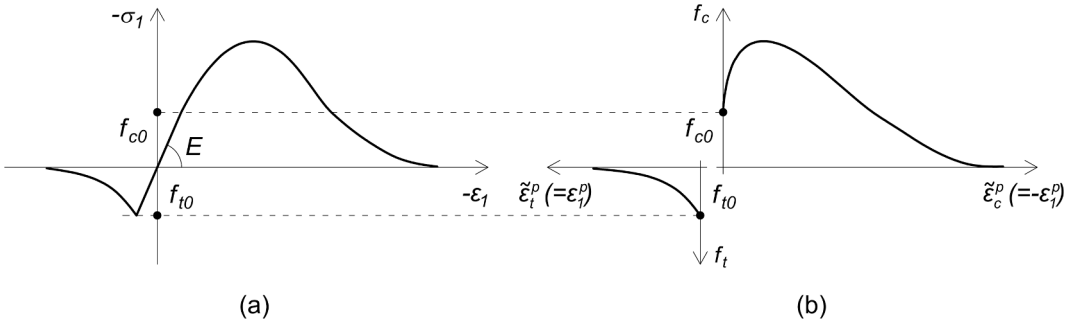

Fig. A1. Evolution of the yield function in the plastic regime under uniaxial loading: (a) stress-strain curve; (b) stress-effective plastic strain curve.

Appendix B

This section summarises the force and moment equilibrium equations governing the response at failure of free-head (Fig. 14) and fixed-head (Fig. 15) piles.

- Free-Head short pile

$$\overline{H}_u = \frac{\overline{p}_{u0} + \overline{p}_{u,2D}}{2}\overline{z}_{lim} + \overline{p}_{u,2D}(\overline{f} - \overline{z}_{lim}) \tag{B1a}$$

$$-\overline{H}_u(\overline{e} + \overline{f} + \overline{g}) + \overline{p}_{u,2D}\overline{g}^2 + \overline{p}_{u,2D}\overline{f}\left(\frac{\overline{f}}{2} + \overline{g}\right) - \frac{\overline{p}_{u,2D} - \overline{p}_{u0}}{2}\overline{z}_{lim}\left(\overline{f} + \overline{g} - \frac{\overline{z}_{lim}}{3}\right) = 0 \tag{B1b}$$

$$\overline{g} = \frac{\overline{L} - \overline{f}}{2} \tag{B1c}$$

- Free-Head long pile

If $\overline{f} \le \overline{z}_{lim}$:

$$\overline{H}_u = \frac{2\overline{p}_{u0} + \overline{m}\overline{f}}{2}\overline{f} \tag{B2a}$$

$$\overline{M}_{yb} - \overline{H}_u\left(\overline{e} + \overline{f}\frac{3\overline{p}_{u0} + 2\overline{m}\overline{f}}{6\overline{p}_{u0} + 3\overline{m}\overline{f}}\right) = 0 \tag{B2b}$$

else, if $\overline{f} > \overline{z}_{lim}$:

$$\overline{H}_u = \frac{\overline{p}_{u0} + \overline{p}_{u,2D}}{2}\overline{z}_{lim} + \overline{p}_{u,2D}(\overline{f} - \overline{z}_{lim}) \tag{B3a}$$

$$\overline{M}_{yb} - \overline{H}_u\overline{e} - \frac{\overline{p}_{u0} + 2\overline{p}_{u,2D}}{6}\overline{z}_{lim}^2 - \frac{\overline{p}_{u,2D}}{2}(\overline{f}^2 - \overline{z}_{lim}^2) = 0 \tag{B3b}$$

- Fixed-Head short pile

$$\overline{H}_u = \frac{(\overline{p}_{u0} + \overline{p}_{u,2D})}{2}\overline{z}_{lim} + \overline{p}_{u,2D}(\overline{L} - \overline{z}_{lim}) \tag{B4}$$

- Fixed-Head intermediate pile

$$\overline{H}_u = \frac{\overline{p}_{u0} + \overline{p}_{u,2D}}{2}\overline{z}_{lim} + \overline{p}_{u,2D}(\overline{f} - \overline{z}_{lim}) \tag{B5a}$$

$$\overline{M}_{yb} - \overline{H}_u(\overline{f} + \overline{g}) + \overline{p}_{u,2D}\overline{g}^2 + \overline{p}_{u,2D}\overline{f}\left(\frac{\overline{f}}{2} + \overline{g}\right) - \frac{\overline{p}_{u,2D} - \overline{p}_{u0}}{2}\overline{z}_{lim}\left(\overline{f} + \overline{g} - \frac{\overline{z}_{lim}}{3}\right) = 0 \tag{B5b}$$

- Fixed-Head long pile

If $\overline{f} \le \overline{z}_{lim}$:

$$\overline{H}_u = \frac{2\overline{p}_{u0} + \overline{m}\overline{f}}{2}\overline{f} \tag{B6a}$$

$$2\overline{M}_{yb} - \overline{H}_u\overline{f}\frac{3\overline{p}_{u0} + 2\overline{m}\overline{f}}{6\overline{p}_{u0} + 3\overline{m}\overline{f}} = 0 \tag{B6b}$$

else, if $\overline{f} > \overline{z}_{lim}$:

$$\overline{H}_u = \frac{\overline{p}_{u0} + \overline{p}_{u,2D}}{2}\overline{z}_{lim} + \overline{p}_{u,2D}(\overline{f} - \overline{z}_{lim}) \tag{B7a}$$

$$2\overline{M}_{yb} - \frac{\overline{p}_{u0} + 2\overline{p}_{u,2D}}{6}\overline{z}_{lim}^2 - \frac{\overline{p}_{u,2D}}{2}(\overline{f}^2 - \overline{z}_{lim}^2) = 0 \tag{B7b}$$

References

ABAQUS, Inc.. ABAQUS 2017 User's Manual. Dassault Systèmes Simulia Corp (2017).

Broms, B.B. (1964a). Lateral resistance of piles in cohesive soils. Journ. Soil Mech. Found. Div., Proc. ASCE, vol. 90, SM2, pp. 27-63.

Broms, B.B. (1964b). Lateral resistance of piles in cohesionless soils. Journ. Soil Mech. Found. Div., Proc. ASCE, vol. 90, SM3, pp. 123-156.

Cecconi, M., Pane, V., Vecchietti, A., Bellavita, D., 2019. Horizontal capacity of single piles: An extension of Broms' theory for c-ϕ soils. Soils Found. 59 (4), 840–856. https://doi.org/10.1016/j.sandf.2019.01.007.

Ceresa, P., Petrini, L., Pinho, R., 2007. Flexure-shear fiber beam-column elements for modeling frame structures under seismic loading – state of the art. J. Earthq. Eng. 11 (S1), 46–88.

Chen, Y J, and Kulhawy, F H. 1994. "Case history evaluation of the behavior of drilled shafts under axial and lateral loading. Final report". United States.

Chen, Y.J., Lin, S.S., Chang, H.W., Marcos, M.C., 2011. Evaluation of side resistance capacity for drilled shafts. J. Mar. Sci. Technol. 19 (2), 13.

Comodromos, E.M., Papadopoulou, M.C., 2012. Response evaluation of horizontally loaded pile groups in clayey soils. Géotechnique 62 (4), 329–339.

Comodromos, E.M., Pitilakis, K.D., 2005. Response evaluation for horizontally loaded fixed-head pile groups using 3-D non-linear analysis. Int. J. Numer. Anal. Meth. Geomech. 29 (6), 597–625.

Conte, E., Troncone, A., Vena, M., 2013. Nonlinear three-dimensional analysis of reinforced concrete piles subjected to horizontal loading. Comput. Geotech. 49, 123–133.

Conte, E., Troncone, A., Vena, M., 2015. Behaviour of flexible piles subjected to inclined loads. Comput. Geotech. 69, 199–209.

Duvaut, G., Lions, J. (1972). Les inéquations en méchanique et en physique, Dunod, Paris.

Georgiadis, K., 2014. Variation of limiting lateral soil pressure with depth for pile rows in clay. Comput. Geotech. 62, 164–174.

Georgiadis, K., Georgiadis, M., 2010. Undrained lateral pile response in sloping ground. J. Geotech. Geoenviron. Eng. 136 (11), 1489–1500.

Gerolymos, N., Giannakos, S., Drosos, V., 2020. Generalised failure envelope for laterally loaded piles: Analytical formulation, numerical verification and experimental validation. Geotechnique 70 (3), 248–267.

Kulhawy, F. H. (1991). Drilled shaft foundations. In Foundation engineering handbook (pp. 537-552). Boston, MA: Springer US.

Lalicata, L.M., Bruno, A.W., Gallipoli, D., 2023. An extension of Broms' theory to unsaturated soils. Comput. Geotech. 155, 105189.

Lee, J., Fenves, G.L., 1998. Plastic-damage model for cyclic loading of concrete structures. J. Eng. Mech. 124 (8), 892–900.

Lubliner, J., Oliver, J., Oller, S., Oñate, E., 1989. A plastic-damage model for concrete. Int. J. Solids Struct. 25 (3), 299–326.

Luo, R., Zhu, B., Yang, Z., 2021. Limiting force profile for laterally loaded piles in undrained clay. Int. J. Geomech. 21 (8), 04021146.

Martin, C.M., Randolph, M.F., 2006. Upper-bound analysis of lateral pile capacity in cohesive soil. Géotechnique 56 (2), 141–145. https://doi.org/10.1680/geot.2006.56.2.141.

Matlock, H. (1970). Correlations for design of laterally loaded piles in soft clay. In Vol. 1 of Proc., 2nd Offshore Technology Conf., 577–594. Houston: OTC.

Murff, J.D., Hamilton, J.M., 1993. P-Ultimate for undrained analysis of laterally loaded piles. J. Geotech. Eng. 119 (1), 91–107. https://doi.org/10.1061/(ASCE)0733-9410(1993)119:1(91).

Papadopoulou, M.C., Comodromos, E.M., 2010. On the response prediction of horizontally loaded fixed-head pile groups in sands. Comput. Geotech. 37 (7–8), 930–941.

Phoon, K.K., Kulhawy, F.H., 2005. Characterisation of model uncertainties for laterally loaded rigid drilled shafts. Geotechnique 55 (1), 45–54.
Psychari, A., Anastasopoulos, I., 2022. Combined loading of RC pile groups in clay accounting for N-M interaction. Soil Dyn. Earthq. Eng. 163, 107490.
Randolph, M.F., Houlsby, G.T., 1984. The limiting pressure on a circular pile loaded laterally in cohesive soil. Géotechnique 34 (4), 613–623. https://doi.org/10.1680/geot.1984.34.4.613.
Reese, L. C., Cox, W. R. & Koop, F. D. (1975). Field testing and analysis of laterally loaded piles in stiff clay. In Proc., 7th Annual OTC, 672–690. Richardson, TX: OnePetro.
Sakellariadis, L., Anastasopoulos, I., 2022. On the mechanisms governing the response of pile groups under combined VHM loading. Géotechnique. https://doi.org/10.1680/jgeot.21.00236.
Sakellariadis, L., Anastasopoulos, I., 2024. Analytical 3D failure envelopes for RC pile groups under combined loading: A generalised design approach. Soil Dyn. Earthq. Eng. 181, 108570.
Sakellariadis, L., Anastasopoulos, I., Gazetas, G., 2020. Fukae bridge collapse (Kobe 1995) revisited: New insights. Soils Found. 60 (6), 1450–1467.
Tzivakos, K.P., Kavvadas, M.J., 2014. Numerical investigation of the ultimate lateral resistance of piles in soft clay. Front. Struct. Civ. Eng. 8 (2), 194–200.
Yu, J., Huang, M., Zhang, C., 2015. Three-dimensional upper-bound analysis for ultimate bearing capacity of laterally loaded rigid pile in undrained clay. Can. Geotech. J. 52 (11), 1775–1790. https://doi.org/10.1139/cgj-2014-0390.